Astronomy & Astrophysics

Characterization of star-forming dwarf galaxies at 0.1 ≲ z ≲ 0.9 in VUDS: probing the low-mass end of the mass-metallicity relation[⋆]

A. Calabrò[1,2], R. Amorín[1,3,4], A. Fontana[1], E. Pérez-Montero[12], B. C. Lemaux[13], B. Ribeiro[5], S. Bardelli[8],
M. Castellano[1], T. Contini[9,10], S. De Barros[11], B. Garilli[6], A. Grazian[1], L. Guaita[1], N. P. Hathi[5,14],
A. M. Koekemoer[14], O. Le Fèvre[5], D. Maccagni[6], L. Pentericci[1], D. Schaerer[11,9], M. Talia[7],
L. A. M. Tasca[5], and E. Zucca[8]

[1] INAF–Osservatorio Astronomico di Roma, via di Frascati 33, 00040 Monte Porzio Catone, Italy
[2] Laboratoire AIM-Paris-Saclay, CEA/DSM-CNRS-Université Paris Diderot, Irfu/Service d' Astrophysique, CEA Saclay, Orme des Merisiers, 91191 Gif sur Yvette, France
e-mail: antonello.calabro@cea.fr
[3] Cavendish Laboratory, University of Cambridge, 19 JJ Thomson Avenue, Cambridge, CB3 0HE, UK
[4] Kavli Institute for Cosmology, University of Cambridge, Madingley Road, Cambridge CB3 0HA, UK
[5] Aix-Marseille Université, CNRS, LAM (Laboratoire d'Astrophysique de Marseille) UMR 7326, 13388 Marseille, France
[6] INAF–IASF, via Bassini 15, 20133 Milano, Italy
[7] University of Bologna, Department of Physics and Astronomy (DIFA), viale Berti Pichat 6/2, 40127 Bologna, Italy
[8] INAF–Osservatorio Astronomico di Bologna, via Ranzani 1, 40127 Bologna, Italy
[9] IRAP, Institut de Recherche en Astrophysique et Planétologie, CNRS, 14 avenue Édouard Belin, 31400 Toulouse, France
[10] Université de Toulouse, UPS-OMP, 31400 Toulouse, France
[11] Geneva Observatory, University of Geneva, ch. des Maillettes 51, 1290 Versoix, Switzerland
[12] Instituto de Astrofísica de Andalucía. CSIC. Apartado de correos 3004, 18080 Granada, Spain
[13] Department of Physics, University of California, Davis, One Shields Ave., Davis, CA 95616, USA
[14] Space Telescope Science Institute, 3700 San Martin Drive, Baltimore, MD 21218, USA

ABSTRACT

Context. The study of statistically significant samples of star-forming dwarf galaxies (SFDGs) at different cosmic epochs is essential for the detailed understanding of galaxy assembly and chemical evolution. However, the main properties of this large population of galaxies at intermediate redshift are still poorly known.
Aims. We present the discovery and spectrophotometric characterization of a large sample of 164 faint ($i_{AB} \sim 23$–25 mag) SFDGs at redshift $0.13 \leq z \leq 0.88$ selected by the presence of bright optical emission lines in the VIMOS Ultra Deep Survey (VUDS). We investigate their integrated physical properties and ionization conditions, which are used to discuss the low-mass end of the mass-metallicity relation (MZR) and other key scaling relations.
Methods. We use optical VUDS spectra in the COSMOS, VVDS-02h, and ECDF-S fields, as well as deep multi-wavelength photometry that includes HST-ACS *F814W* imaging, to derive stellar masses, extinction-corrected star-formation rates (SFR), and gas-phase metallicities of SFDGs. For the latter, we use the direct method and a T_e-consistent approach based on the comparison of a set of observed emission lines ratios with the predictions of detailed photoionization models.
Results. The VUDS SFDGs are compact (median $r_e \sim 1.2$ kpc), low-mass ($M_* \sim 10^7$–10^9 $M_\odot$) galaxies with a wide range of star-formation rates ($SFR(H\alpha) \sim 10^{-3}$–$10^1$ $M_\odot$/yr) and morphologies. Overall, they show a broad range of subsolar metallicities (12 + log(O/H) = 7.26–8.7; $0.04 \lesssim Z/Z_\odot \lesssim 1$). Nearly half of the sample are extreme emission-line galaxies (EELGs) characterized by high equivalent widths and emission line ratios indicative of higher excitation and ionization conditions. The MZR of SFDGs shows a flatter slope compared to previous studies of galaxies in the same mass range and redshift. We find the scatter of the MZR is partly explained in the low mass range by varying specific SFRs and gas fractions amongst the galaxies in our sample. In agreement with recent studies, we find the subclass of EELGs to be systematically offset to lower metallicity compared to SFDGs at a given stellar mass and SFR, suggesting a younger starburst phase. Compared with simple chemical evolution models we find that most SFDGs do not follow the predictions of a "closed-box" model, but those from a gas-regulating model in which gas flows are considered. While strong stellar feedback may produce large-scale outflows favoring the cessation of vigorous star formation and promoting the removal of metals, younger and more metal-poor dwarfs may have recently accreted large amounts of fresh, very metal-poor gas, that is used to fuel current star formation.

Key words. galaxies: evolution – galaxies: high-redshift – galaxies: dwarf – galaxies: abundances – galaxies: starburst

---

1. Introduction

Low-mass (dwarf) galaxies are the most abundant systems of the Universe at all cosmic epochs, as shown by catalogs of nearby

galaxies (Karachentsev et al. 2004) and by the steepness of the galaxy stellar mass (M_*) function at $M_* < 10^{10}\ M_\odot$ up to high redshift (Fontana et al. 2006; Santini et al. 2012; Grazian et al. 2015). The most commonly accepted definition of dwarf galaxies refers to low-mass ($M_* < 10^9\ M_\odot$) and low-luminosity systems with $M_i - 5\log h_{100} > -18$ (Sánchez-Janssen et al. 2013). They are considered the building blocks from which more massive galaxies form (Press & Schechter 1974). This assembly process is not constant, but it peaks at $z \sim 2$ and then declines exponentially at later times (e.g., Madau & Dickinson 2014). Almost 25% of the stellar mass observed today has been assembled after this peak, and a significant part of it formed in young low-mass galaxies in strong, short-lived starbursts (Guzmán et al. 1997; Kakazu et al. 2007). Some of these star-forming low-mass galaxies also show bright emission lines in their optical rest-frame spectra, due to photoionization of the nebula surrounding hot massive (O type) stars. This makes them easier to identify even beyond the local Universe in current spectroscopic surveys. Throughout this paper, we refer to this kind of faint galaxy with bright emission lines detected in the optical ([O II], [O III], Hβ and Hα) as star-forming dwarf galaxies (SFDG). Among them, a particular subset is represented by extreme emission line galaxies (EELG), which are selected by the high equivalent width (EW) of their optical emission lines (EW[O III] > 100–200 Å), and have more extreme properties; for example, higher surface densities, lower starburst ages, and lower gas metallicities than the average population of star-forming dwarfs (Kniazev et al. 2004; Cardamone et al. 2009; Amorín et al. 2010, 2012, 2014, 2015; Atek et al. 2011; van der Wel et al. 2011; Maseda et al. 2014). While the population of EELGs itself constitutes an ideal laboratory for studying star formation and chemical enrichment under extreme physical conditions, it also appears to contain environments that most closely resemble "typical" galaxies at very high redshifts ($z \gtrsim 3$–4, e.g., Smit et al. 2014; Stark et al. 2017).

Tracing the galaxy-averaged properties of large, representative samples of star-forming dwarf galaxies (SFDGs) since $z \sim 1.5$ is a necessary step for gaining a complete understanding of the evolution of low-mass galaxies and the build-up of stellar mass during the last 9−10 billion years. How SFDGs assemble their stellar mass remains one of the unanswered questions surrounding these galaxies. Differently from high-mass ($M_* > 10^9\ M_\odot$) galaxies, which show a continuous rate of star formation (SF), the most common scenario for dwarf galaxies is the cyclic bursty mode, as pointed out by theoretical models (e.g., Hopkins et al. 2014; Sparre et al. 2017) and observations (Guo et al. 2016b). Intense SF episodes produce stellar feedback through strong winds and supernova, which heat and expel the surrounding gas in outflows, eventually resulting in a temporary quenching of SF on timescales of tens of Myr (e.g., Olmo-Garcia et al. 2017; Pelupessy et al. 2004). Then, the metal-enriched gas may be accreted back to the galaxy triggering new SF episodes. The scaling relation between stellar mass M_* and SF rate ($SFR = M_*$ produced per year) can be used to compare the assembly dynamics of different types of galaxies. For high-mass ($M_* > 10^9\ M_\odot$) star-forming galaxies a tight correlation was found between the two quantities at all redshifts from $z = 0$ to $z = 5$, called the main sequence (MS) of star-formation (Brinchmann et al. 2004; Noeske et al. 2007; Daddi et al. 2007; Tasca et al. 2015). This sequence moves towards higher SFRs at higher z, though its slope remains almost constant ($\sim$1) (Guo et al. 2015). At lower masses, SFDGs and, in particular, those with the strongest emission lines (EELGs) are found to have increased SFRs at fixed M_* (by $\sim$1 dex) compared to the extrapolation at low mass of the MS (Amorín et al. 2015),

suggesting that they are efficiently forming stars in strong bursts with stellar mass doubling times <1 Gyr, which cannot be sustained for long.

The mechanisms regulating galaxy growth, such as gas accretion and SF feedback are still not completely understood, and the scarcity of direct observations of outflows and gas accretion (as well as a quantification of their rate) represent a limit to a deeper insight (Sánchez Almeida et al. 2014a). However, since the stellar-mass build-up in galaxies is accompanied by the chemical enrichment of their interstellar medium (ISM), studying the gas-phase metallicity and its relation with stellar mass and SFR can help us to investigate which of these processes are playing major roles. Thus, the gas-phase metallicity (defined as the oxygen abundance, $12 + \log(\text{O/H})$) is found to tightly correlate with stellar mass (e.g., Lequeux et al. 1979; Tremonti et al. 2004) up to high redshift ($z \sim 3.5$, e.g., Maiolino et al. 2008; Zahid et al. 2012a; Cullen et al. 2014; Troncoso et al. 2014; Onodera et al. 2016), with a relatively steep slope flattening above $10^{10.5}\ M_\odot$. The normalization of this mass-metallicity relation (MZR) appears to evolve to lower metallicities with increasing redshift at fixed stellar mass (Savaglio 2010; Shapley et al. 2005; Erb et al. 2006; Maiolino et al. 2008; Mannucci et al. 2009), while the slope, especially in its low-mass end, is still not constrained (e.g., Christensen et al. 2012; Henry et al. 2013; Whitaker et al. 2014; Salim et al. 2014). However, both the slope and normalization of the MZR have been found to strongly depend on the method used to derive metallicity (Kewley & Ellison 2008). The largest discrepancies (as high as 0.7 dex) are between metallicities measured using the direct method and strong line methods. The former is also known as the T_e method, because it is based on measurement of the electron temperature (T_e) of the ionized gas, which requires measurements of weak auroral lines, such as [O III]λ4363 (e.g., Hägele et al. 2008; Curti et al. 2017). The latter, instead, are based on empirical or model-based calibrations of bright emission line ratios as a function of metallicity.

At lower masses ($M_* < 10^9\ M_\odot$), the mass-metallicity relation is still not completely characterized. Among the various studies that have tried to investigate whether or not a correlation exists at lower masses, Lee et al. (2006) (L06) derived a T_e-consistent MZR from 27 nearby ($D \le 5$ Mpc) star-forming dwarf galaxies (down to $M_* \sim 10^6\ M_\odot$), with a low scatter (± 0.117 dex). Using stacked spectra from the SDSS-DR7, Andrews & Martini (2013) (AM13) measured T_e from weak auroral lines and used the direct method to derive metallicities over approximately 4 decades in stellar mass and study the MZR. They found that the MZR has a sharp increase (O/H $\propto M_*^{1/2}$) from $\log(M_*) = 7.4$ to $\log(M_*) = 8.9\ M_\odot$, and flattens at $\log(M_*) = 8.9\ M_\odot$. Above this value, the MZR derived from the direct method reaches an asymptotic metallicity of $12 + \log(\text{O/H}) = 8.8$. Zahid et al. (2012b) studied the mass-metallicity relation down to $10^7\ M_\odot$, showing that the scatter increases towards lower stellar masses. In a series of papers, Ly et al. (2014, 2015, 2016b) studied 20, 28 and 66 emission line galaxies, respectively, with stellar masses <$10^9\ M_\odot$ out to $z \sim 0.9$. In all cases they reported detection of the O4363 Å auroral line (and significant upper limits for 98 additional sources), which allow them to derive metallicities and investigate the MZR using the direct method. In their latest work, they find that their MZR is consistent with AM13 at $z \lesssim 0.3$, and evolves toward lower abundances at increasing redshifts. Recently, Guo et al. (2016a) performed a statistically significant analysis of the MZR at $z \sim 0.5$–0.7 down to 10^8 solar masses using a sample of

1381 galaxies collected from deep surveys, 237 of them with $M_* < 10^9$ $M_\odot$, which implied ~10 times larger than previous studies at similar stellar masses and redshift. While they do not present O4363 Å detections, their statistical study relies on metallicity estimates using the [O III]λ5007/Hβ line ratio and empirical calibrations (Maiolino et al. 2008). Their MZR has a shallower slope than AM13, which is in agreement with theoretical predictions incorporating supernova energy-driven winds (Dekel & Woo 2003; Davé et al. 2012; Forbes et al. 2014), and they find an increasing scatter toward lower masses, up to 0.3 dex at $M_* \sim 10^8$ $M_\odot$.

The correlation between stellar mass and metallicity is a natural consequence of the conversion of gas into stars within galaxies, regulated by gas exchanges with the environment through inflows or outflows, but we still don't know exactly which processes influence the shape, normalization and scatter of this relation. Besides observations, semi-analytical models and cosmological hydrodynamic simulations including chemical evolution have tried to explain the observed MZR. According to Kobayashi et al. (2007) and Spitoni et al. (2010), the galactic winds can easily drive metals out of low-mass galaxies due to their lower potential wells. In other studies, dwarf galaxies have longer timescales of conversion (regulated by galactic winds) from gas reservoirs to stars, so they are simply less evolved and less enriched systems (Finlator & Davé 2008). The models proposed by Tassis et al. (2008) introduce a critical density threshold for the activation of star-formation, without requiring outflows to reduce the star formation efficiency and the metal content. Finally, the observed MZR can be explained assuming accretion of metal-poor gas along filaments from the cosmic web (cold-flows) (e.g., Dalcanton et al. 2004; Ceverino et al. 2015; Sánchez Almeida et al. 2014b), for which also indirect evidences have been found in recent observations (Sánchez Almeida et al. 2015).

Lastly, SFDGs are important because among them we find analogs of high redshift galaxies, which typically show high sSFRs, low metallicity, high ionization in terms of [O III]λ5007/[O II]λ3727 and compact sizes (Izotov et al. 2015). Recent work by Stasińska et al. (2015) shows that EELGs are characterized by [O III]λ5007/[O II]λ3727 > 5, reaching values up to 60 in some of them, allowing radiation to escape and ionize the surrounding ISM (Nakajima & Ouchi 2014). Such types of galaxies at high redshift are thought to significantly contribute to the reionization of the Universe, providing up to 20% of the total ionizing flux at $z \sim 6$ (Robertson et al. 2015; Dressler et al. 2015). As far as the sizes are concerned, SFDGs selected by strong optical emission lines (in particular [O III]λ5007) are typically small isolated systems with radii of the order of ~1 kpc (Izotov et al. 2016) and they show irregular morphologies (Amorín et al. 2015).

This paper presents a characterization of the main integrated physical properties of a large and representative sample of 164 star-forming dwarf galaxies at 0.13 < z < 0.88 drawn from the VIMOS Ultra-Deep Survey[1] (VUDS, Le Fèvre et al. 2015). By construction, VUDS has two important advantages compared to previous surveys (e.g., zCOSMOS): (i) its unprecedented depth due to long integrations, which allows us to probe very faint targets $I_{AB} \sim 23-25$ at $z < 1$; and (ii) a large area, covering three deep fields, COSMOS, ECDFS, and VVDS-02h, for which a wealth of ancillary multi-wavelength data is available.

These advantages are particularly important for the main goal of this paper: to investigate the metallicity and ionization of galaxies with M_* as low as 10^7 $M_\odot$ and the relation with their stellar mass, star-formation rates, and sizes.

We derive galaxy-averaged metallicity and ionization parameters for the entire sample using a new robust χ^2 minimization code called HII-CHI-mistry (HCm, Pérez-Montero 2014), based on the comparison of detailed photoionization models and observed optical line ratios. HCm is particularly efficient because it gives results that are consistent with the direct method in the entire metallicity range spanned by our sample, even in the absence of an auroral line detection (e.g., [O III]λ4363). For most galaxies, we use space-based (HST-ACS) images to study their morphological properties and quantify galaxy sizes, allowing us to compare with other samples of SFDGs and study their impact on the mass-metallicity and the other scaling relations.

Our paper is organized as follows. In Sect. 2, we describe the parent VUDS sample, the parent photometric catalogs and the SDSS data used in this paper for comparison. In Sect. 3, we describe the selection criteria adopted to compile our sample of SFDGs, followed by the details on emission line measurements and AGN removal. In Sect. 4 we describe the main physical properties (stellar masses, star-formation rates, morphology and sizes, metallicity and ionization) of the sample and the methodology used to derive all of them. In Sect. 5, we present our main results and we study empirical relations between different properties, in particular the mass-metallicity relation. We also compare the results with similar samples of star-forming dwarf galaxies at low and intermediate redshift. In Sect. 6, we discuss our results, with the implications on galaxy stellar mass assembly. We compare our findings to the predictions of simple chemical evolution models, and provide a sample of Lyman-continuum galaxy candidates for reionization studies. Finally, we show the summary and conclusions in Sect. 7, while, in an Appendix, we provide tables with all our measurements and compare the metallicities derived with HCm with those obtained using well-know strong-line calibrations, and study the effects on the MZR.

Throughout this paper we adopt a standard Λ-CDM cosmology with $h = 0.7$, $\Omega_m = 0.3$ and $\Omega_\Lambda = 0.7$. All EWs are presented in the rest-frame. We adopt $12 + \log(O/H) = 8.69$ as the solar oxygen abundance (Asplund et al. 2009).

2. Observations

2.1. The parent VUDS sample and redshift measurement

VUDS (Le Fèvre et al. 2015) is a spectroscopic redshift survey observing approximately 10 000 galaxies to study the major phase of galaxy assembly up to redshift $z \sim 6$. VUDS is one of the largest programs on the ESO-VLT with 640 h of observing time. The survey covers a total of one square degree in three separate fields to reduce the impact of cosmic variance: the COSMOS field, the extended Chandra Deep Field South (ECDFS), and the VVDS-02h field. All the details about the survey strategy, target selection, data reduction and calibrations, and redshift measurements can be found in Le Fèvre et al. (2015) and Tasca et al. (2017). Below we briefly summarize the survey features that are relevant to the present study.

The spectroscopic observations were carried out at the VLT with the VIMOS Multi-Object Spectrograph (MOS), which has a wide field of 224 arcmin[2] (Le Fèvre et al. 2003). The spectrograph is equipped with slits 1″ wide and 10″ long, as well as two grisms (LRBLUE and LRRED) covering a wavelength range of 3650 < λ < 9350 Å at uniform spectral resolution of

$R = 180$ and $R = 210$, respectively. This allows us to observe the Lyman-α line at $\lambda 1215$ Å up to redshift $z \sim 6.6$, and also Hβ, [O II]$\lambda\lambda 3727$, 3729, and [O III]$\lambda\lambda 4959$, 5007 emission lines for galaxies at $z \lesssim 0.88$. The integration time (on-source) is $\simeq 14$ h per target for each grism, which allows us to detect the continuum at 8500 Å for $i_{AB} = 25$, and emission lines with an observed flux limit $F = 1.5 \times 10^{-18}$ erg s^{-1} cm^{-2} at $S/N \sim 5$.

Redshift measurements in VUDS were performed using the EZ code (Garilli et al. 2010), both in automatic and manual modes for each spectrum, supervised independently by two persons. Different flags have been assigned to each galaxy according to the probability of the measurement being correct, with flags 3 and 4 as those with the highest ($\geq 95\%$) probability of being correct. The overall redshift accuracy is $dz/(1 + z) = 0.0005$–0.0007 (or an absolute velocity accuracy of 150–200 km s^{-1}). The redshift distribution of the VUDS parent sample shows the majority of galaxies at redshift $z_{spec} > 2$, while there is a lower redshift tail peaking at $z_{spec} \simeq 1.5$, which represents approximately 20% of the total number of targets.

2.2. The parent photometric catalogs

The three fields of the VUDS survey (COSMOS, ECDFS and VVDS-02h) benefit of plenty of deep multi-wavelength data, which are fundamental in combination with the spectroscopic redshifts in order to derive important physical quantities of galaxies, such as stellar masses, absolute magnitudes, and SED-based star-formation rates.

In the COSMOS field (Scoville et al. 2007), GALEX near-UV (2310 Å) and far-UV (1530 Å) magnitudes are available down to $m_{AB} = 25.5$ (Zamojski et al. 2007). Extensive imaging observations were carried out with the Subaru Suprime-Cam in $BVgriz$ broad-bands by Taniguchi et al. (2007) down to $i_{AB} \sim 26.5$ mag, as well as with CFHT Megacam in the u-band by Boulade et al. (2003). The ULTRA-VISTA survey acquired very deep near-infrared imaging in the $YJHK$ bands with 5σAB depths of ~ 25 in Y and ~ 24 in JHK bands.

The ECDFS field has been studied by a wealth of photometric surveys as well. All the photometry in this field is taken from Cardamone et al. (2010), who observed with Subaru Suprime-Cam in 18 optical medium-band filters (down to $R_{AB} \sim 25.3$) as part of the MUSYC survey (Gawiser et al. 2006). They also created a uniform catalog combining their observations with ancillary photometric data available in MUSYC. They comprise $UBVRIz'$ bands from Gawiser et al. (2006), JHK from Taylor et al. (2009) and Spitzer IRAC photometry (3.6 μm, 4.5 μm, 5.8 μm, 8.0 μm) from the SIMPLE survey (Damen et al. 2011).

The VVDS-02h field was observed with $u*g'r'i'z'$ filters as part of CFHT Legacy Survey (CFHTLS[2]) by Cuillandre et al. (2012), reaching $i_{AB} = 25.44$. Deep infrared photometry is also available in $YJHK$ bands from WIRCAM at CFHT (Bielby et al. 2012) down to $K_{AB} = 24.8$, and in the 3.6 μm and 4.5 μm Spitzer bands thanks to the SERVS survey (Mauduit et al. 2012). For the VVDS-02h and the ECDFS fields, GALEX photometry is not available.

In addition, for the COSMOS and ECDFS field, we have HST-ACS images in $F814W$, $F125W$, and $F160W$ bands from Koekemoer et al. (2007). The typical spatial resolution of these images are $\sim 0.09''$ for the $F814W$ band (0.6 kpc at $z = 0.6$), with a point-source detection limit of 27.2 mag at 5σ. We use

HST images to derive a morphological classification of our galaxies in Sect. 4.4. In contrast, the VVDS-02h field does not have HST coverage. The i' filter images available from CFHT have a lower, seeing-limited spatial resolution of $\sim 0.8''$ (5.4 kpc at $z = 0.6$), implying that the most compact and distant galaxies are not completely resolved in VVDS-02h.

2.3. SDSS data

Throughout this paper we compare our results with those found in the local Universe. For this comparison we use star-forming galaxies coming from the SDSS survey DR7 (Abazajian et al. 2009) and publicly available measurements set by MPA-JHU[3]. We select our SDSS sample by having a redshift ranging $0.02 < z < 0.32$ and signal-to-noise ratio $S/N > 3$ in the following emission lines: [O II] $\lambda\lambda 3727 + 3729$ Å (hereafter [O II]3727), Hβ, [O III] $\lambda 4959$ Å, [O III] $\lambda 5007$ Å, Hα, [N II] $\lambda 6584$ Å and [S II] $\lambda 6717 + 6731$ Å. The stellar masses are derived fitting the photometric data from Stoughton et al. (2002) with Bruzual & Charlot (2003) population synthesis models as described in Kauffmann et al. (2003). The star-formation rates are calculated from Hα luminosities following the method of Brinchmann et al. (2004) and scaled to Chabrier (2003) IMF. They fit $ugriz$ photometry and six emission line fluxes ([O II]3728, Hβ, [O III]4959, [O III]5007, Hα, [N II]6584 and [S II]6717 requiring all $S/N > 3$) with Charlot & Longhetti (2001) models. These are a combination of Bruzual & Charlot (2003) synthetic galaxy SEDs and CLOUDY (Ferland et al. 2013) emission line models, calibrated on the observed ratios of a representative sample of spiral, irregular, starburst and HII galaxies in the local Universe. Finally, the gas-phase metallicity for the SDSS-DR7 comparison sample has been obtained by Amorín et al. (2010) using the N2 calibration of Pérez-Montero & Contini (2009), which was derived using objects with accurate measurements of the electron temperature.

3. Sample selection based on emission lines

3.1. The SFDGs sample selection

In order to define our VUDS sample of SFDGs, we first select in VUDS database[4] a sample of emission-line galaxies with the following selection criteria:

1. high confidence redshift (at least 95% probability of the redshift being correct);
2. Spectroscopic redshift in the range $0.13 < z_{spec} < 0.88$ and magnitudes $i_{AB} > 23$;
3. detection ($S/N \geq 3$) of the following emission lines: [O II] $\lambda 3727$ Å, [O III] $\lambda\lambda 4959$, 5007 Å, Hβ and/or Hα emission lines (we refer to Sect. 3.2 for the emission-line measurements).

The above criteria allow us to select low-luminosity galaxies ($M_i \leq -13.5$ mag) with at least [O III]5007 Å and [O II]3727 Å included in the observed spectral range simultaneously, and derive metallicities and star-formation rates (see Sect. 4). In more detail, the first and second criteria yielded 302 galaxies in COSMOS, 300 in VVDS-02h, and 113 in ECDFS fields. After retrieving all their spectra from the VUDS catalog, we checked them visually, one by one, using IRAF. The final selection and

---
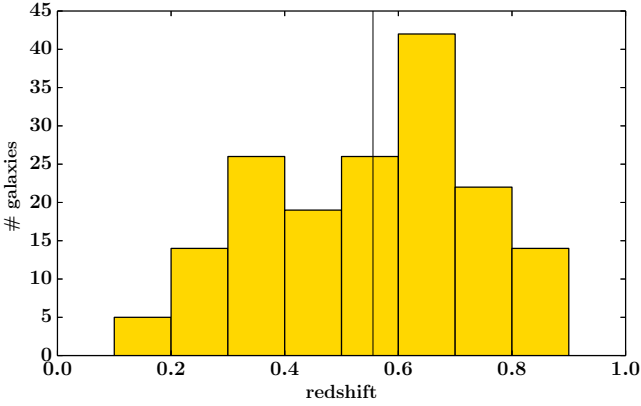
Fig. 1. Redshift distribution of VUDS SFDGs selected from the entire catalog applying the criteria described in Sect. 3.1. The galaxies are binned in intervals of 0.1 in z, and the median redshift distribution ($z_{med} = 0.56$) is represented with a vertical line.

S/N cut was done measuring the emission lines with the methodology presented in Sect. 3.2, excluding the galaxy whenever one of the four emission lines mentioned above ([O II]3727, [O III]4959, 5007, Hβ and/or Hα) was not detected ($S/N < 3$), or appeared contaminated by residual sky emission lines. Applying this procedure, we obtained a final total sample of 168 SFDGs in the redshift range $0.13 < z < 0.88$, with median value $z_{med} = 0.56$ and a vast majority of the galaxies (54%) concentrated between 0.5 and 0.8, as can be seen in the histogram in Fig. 1.

3.2. Emission line measurements

Emission lines fluxes and equivalent widths are measured manually on a one-by-one basis using the task *splot* of IRAF by direct integration of the line profile after linear subtraction of the continuum, which is well detected in all cases. Additionally, we also fit the emission lines of the galaxies with a Gaussian profile. Results using the two approaches are in very good agreement for high S/N emission lines (essentially Hα, Hβ, [O III], and [O II]), while some differences are found for strongly asymmetric or very low S/N ($\sim 3-5$) lines. However, their fluxes and EWs are still consistent within 1σ uncertainties.

We compute uncertainties in the line measurements from the dispersion of values provided by multiple measurements adopting different possible band-passes (free of lines and strong residuals from sky subtraction) for the local continuum determination, which is fitted using a second order polynomial. This approach typically gives larger uncertainties compared to those obtained from the average noise spectrum produced by the data reduction pipeline.

For Balmer lines, the presence of stellar absorption features should also be considered. Even though the faintness of the galaxies does not allow detection of significant absorptions for most of them, we have corrected our measurements upwards by 1 Å in EW of Hγ, Hβ and Hα lines for all galaxies (e.g., Ly et al. 2014). In any case, our galaxies have relatively large EW of Hα and Hβ lines ($EW(H\beta)_{median} = 33$ Å) and the measurement errors are always higher than 1 Å ($\Delta[EW(H\beta)]_{median} = 8$ Å), therefore, this correction must be negligible for our work. In Fig. 2, we show typical spectra for two strong emission-line galaxies in the sample at low- and intermediate-redshift bins, respectively.

As we have described in Sect. 1, a particular class of SFDGs has extreme properties; in particular, a high EW of optical

emission lines. Galaxies with $EW(O III) > 100$ Å are named extreme emission line galaxies (EELGs) according to the definition by Amorín et al. (2015). From our sample, 56% qualify as EELGs (see Fig. 3).

### 3.3. Identification of AGNs: diagnostic diagrams

Galaxies showing emission lines in their spectra include a broad variety of astrophysical objects that can be distinguished according to their excitation mechanisms, that is, thermal (e.g., star formation) or non-thermal (in, e.g., AGN or shocks). AGNs are found in two main categories: broad-line (BL) and narrow-line (NL) AGNs. The former were excluded from the VUDS parent sample before we applied our selection criteria, in order to exclude from the sample any clear AGN candidate for which we still need to identify narrow-line AGNs, such as Seyfert 2 and LINERs. To that end, we used both a cross-correlation of our sample of galaxies with the latest catalogs of X-ray sources and a combination of two empirical diagnostic diagrams based on optical emission-line ratios.

In the ECDFS field, we used the catalogs E-CDFS (Lehmer et al. 2005) and Chandra 4MS (Luo et al. 2008; Xue et al. 2012; Cappelluti et al. 2016). Inside this field, we can exclude AGNs of high and intermediate luminosity (i.e., those with $L_x \geq 10^{43}$ erg s^{-1}). For the COSMOS field, we use the survey Chandra COSMOS (Elvis et al. 2009; Civano et al. 2012) and XMM-COSMOS (Cappelluti et al. 2009), while for the VVDS-02h field we use the catalogs compiled by Pierre et al. (2004) and Chiappetti et al. (2013) from the XMM-LSS survey. Since we have a lower sensitivity for the COSMOS and the VVDS fields compared to the ECDFS field, in those cases we can look for only high luminosity AGNs ($L_x \geq 10^{44}$ erg s^{-1}). We find no X-ray counterpart for any of our VUDS SFDGs in each field observed by the survey.

We inspected the spectra for the presence of very high ionization emission lines (e.g., [NeV]λ3426 Å), very broad components in the Balmer lines, and/or very red SEDs that could suggest the contribution of an AGN, and we did not find any evidence of them.

Finally, we explored two diagnostic diagrams that are frequently used to distinguish between SF, AGN, and galaxies with a combination of different excitation mechanisms (composites). We used adaptations of the classical BPT diagram, that is, the diagnostics of [O III]λ5007/Hβ versus [N II]λ6583/Hα (Baldwin et al. 1981), allowing galaxy classification when Hα and [N II] are no longer observable in optical spectra of intermediate redshift emission-line galaxies. The diagram in Fig. 4 (left) was proposed by Rola et al. (1997) and compares [O II]/Hβ and [O III]/Hβ line ratios. The orange continuous line is the empirical separation (with a 1σ uncertainty of approximately 0.15 dex) derived by Lamareille et al. (2004) between two types of emitting sources: star-forming systems in the bottom left and AGNs in the upper right part.

In Fig. 4 (right), we show the Mass-Excitation (MEx) diagram, introduced by Juneau et al. (2011), which considers the galaxy stellar mass M_* (see Sect. 4.1) instead of the [N II]/Hα ratio, which is available only for ten galaxies from our sample. This diagram relies on the correlation between the line ratio [N II]/Hα and the gas-phase metallicity in SF galaxies (Kewley & Ellison 2008). The empirical relation between mass and metallicity (Tremonti et al. 2004) provides the physical connection between the two quantities. The violet line divides the starburst and AGN regimes and was derived empirically from
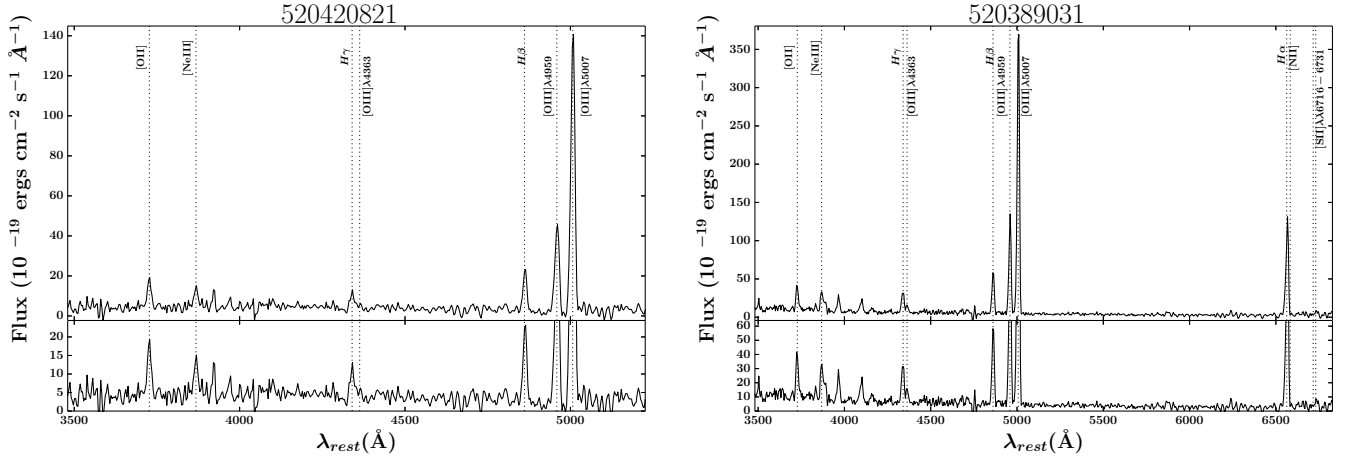
Fig. 2. Observed spectra of two galaxies in VUDS with strong emission lines and faint continuum. The galaxy on the *left and right hand side panels* are at redshift $z = 0.555$ and $z = 0.173$, respectively. While for the former the Hα line lies outside the wavelength range, for the latter it is still visible in the red part of the spectrum. Dotted lines and labels indicate some of the relevant emission lines detected.
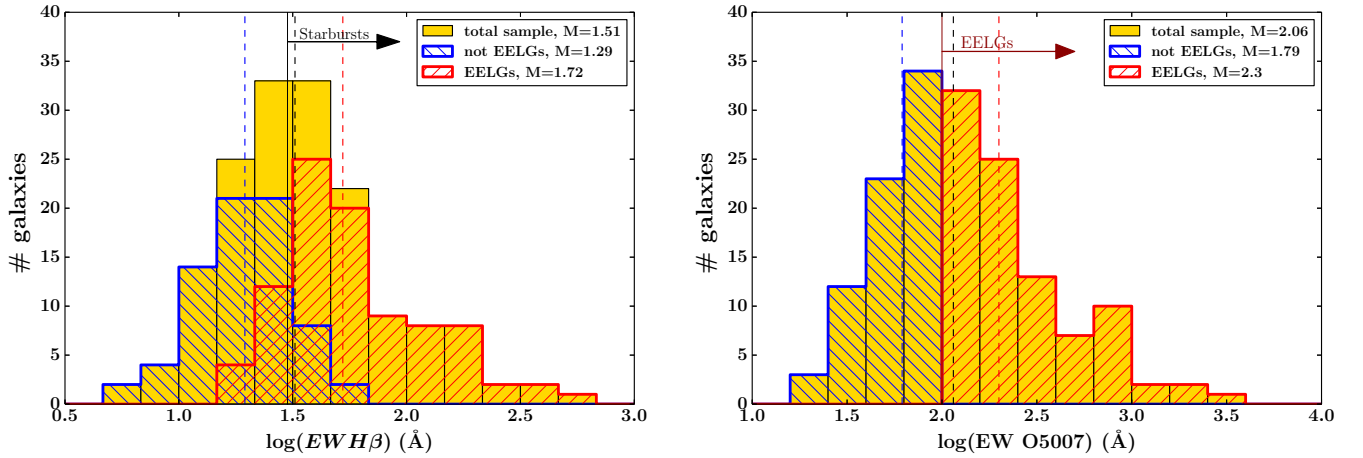
Fig. 3. Distribution of EW(Hβ) and EW(O III) for our sample of galaxies selected in Sect. 3.1. We lined the histogram with different colors; red for the EELG fraction (EW(O III) > 100 Å based on Amorín et al. 2015) and blue for the non-EELG subset. We emphasize, with vertical continuous lines, the empirical limits for starburst galaxies (EW(Hβ) > 30 Å based on Terlevich et al. (1991)) and EELGs, as well as, with vertical dashed lines, the median distribution for the whole sample (black), and the EELGs (red) and non-EELGs (blue) (the values are given in the legend). The standard deviations of the entire distribution are 0.37 and 0.42 for EW(Hβ) and EW(O III), respectively.
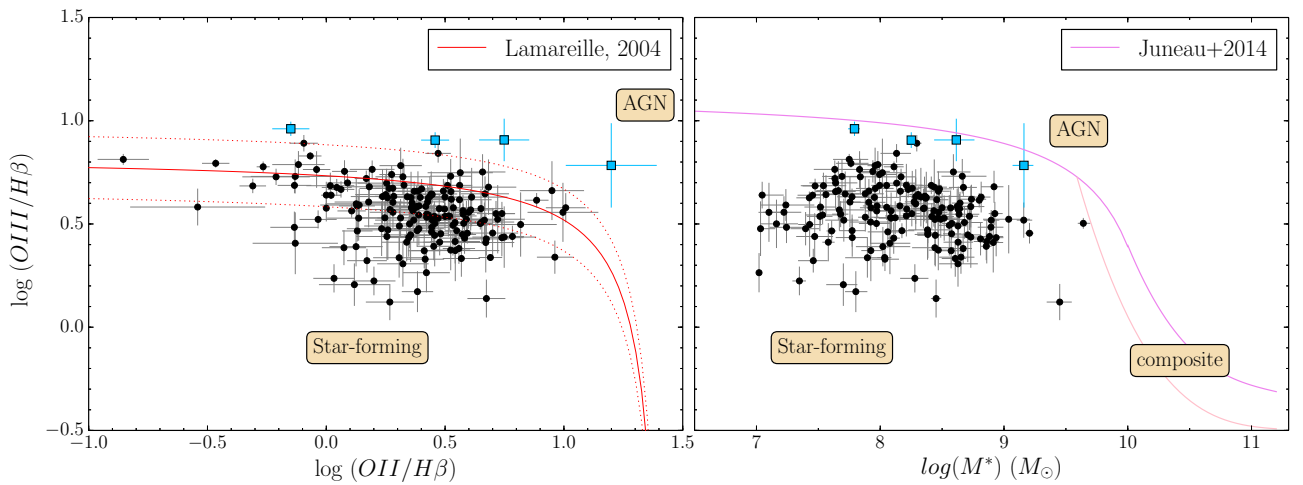
Fig. 4. *Left*: diagnostic diagram to separate SFG, AGN and composite, comparing [O II]λ3727/Hβ and [O III]λ5007/Hβ. The starburst region is in the bottom-left part, while AGNs lie in upper-right part. The red line is the empirical separation by Lamareille et al. (2004) with 0.15 dex uncertainty. *Right*: MEx diagnostic diagram for our sample of emission-line galaxies. The diagram compares the excitation, that is, the emission line ratio [O III]λ5007/Hβ, and the stellar mass M_*. The violet curve is the empirical separation limit between starburst, AGN, and composite regions according to Juneau et al. (2014). In both diagrams, we mark, with blue squares, the four galaxies that lie completely (also including the errors) in the AGN region according to Lamareille et al. (2004).

SDSS emission-line galaxies by Juneau et al. (2014). Below this line, the MEx diagram is populated by star-forming galaxies whose emission lines are powered by stellar photoionization. For this kind of object, models predict an upper limit in the excitation. In the right-upper part, we find AGNs, while in the right-lower part, the region between the two lines is occupied by galaxies showing both star-forming and AGN emission properties (composite). At intermediate redshift ($z \leq 1.5$), star-forming galaxies are consistent with having normal interstellar medium (ISM) properties (Juneau et al. 2011), therefore we can, in principle, apply this diagnostic for all the galaxies in the sample ($z < 0.88$). We also caution the reader that in AGNs, the [N II] line does not trace the metallicity (e.g., Osterbrock 1989) and the connection between the BPT and MEx may not be straightforward. Therefore, we should consider the results of the MEx diagram in combination with other diagnostics that do not suffer from this drawback.

We find that all galaxies are consistent with purely star-forming systems according to the MEx diagram of Juneau et al. (2014), while four galaxies in the [O III]/Hβ versus [O II]/Hβ diagram clearly fall out of the SF region if we consider the 1σ uncertainty ($\sim$0.2 dex) of the empirical relation by Lamareille et al. (2004). In addition, we see a small number of SFDGs with relatively high excitation compared to the empirical limit of Lamareille et al. (2004). It is worth noting that the excitation of objects above those limits does not necessarily require the power of an active nuclear source. A variety of other mechanisms can mimic the properties of AGN in these diagnostics, such as shocks, supernovae, and their subsequent remnants. Indeed, SFDGs (and in particular EELGs) appear to be the preferred sites for the most powerful supernova explosions (Chen et al. 2013; Lunnan et al. 2013; Leloudas et al. 2015; Thöne et al. 2015).

From the combination of the above diagnostics, we find that four galaxies clearly reside in the AGN region of the [O III]/Hβ versus [O II]/Hβ plane of Lamareille et al. (2004), so we exclude them from the following analysis. However, the exclusion or inclusion of these four possible AGN galaxies does not affect any of the results. Indeed, we find that the SFR, metallicity, and gas fractions of these four galaxies are consistent with the median values for the rest of the sample of secure star-forming systems.

After removing the AGN candidates, the subsequent analysis was carried out using 164 SFDGs. The basic information for the galaxies, including redshift and selection magnitude, is presented in Table B.1.

4. Methodology

In Table B.2, which is shown in Appendix B (a complete version is available at the CDS, we present the selected sample of 164 star-forming dwarf galaxies (SFDG) in VUDS. SFDGs are low-mass ($M_* < 10^9 \, M_\odot$), low-luminosity ($M_B > -20$ mag) galaxies that are forming stars at present, as suggested by the presence of optical emission lines, coming from the gas photoionized by newly born massive (O and B) stars. This table also includes measured fluxes (non-extinction corrected) and uncertainties for the most relevant emission lines. These quantities, together with an extended ancillary multiwavelength dataset, are used to derive relevant physical properties of the galaxies, which are presented in Table B.3. In this section, we describe our methodology in detail; we will discuss the results in the following section.

4.1. Stellar masses from multiwavelength SED fitting

We derive stellar masses from SED fitting performed on the available multi-wavelength photometric data using the code Le Phare (Ilbert et al. 2006), as described in Ilbert et al. (2013). In brief, the code uses a chi-square minimization routine, fitting, for each galaxy, Bruzual & Charlot (2003) stellar population synthesis models to all broadband photometric data available in each VUDS field (COSMOS, ECDFS, and VVDS-02h) between GALEX far-UV and Spitzer 4.5 μm band, presented in Sect. 2.2. The models include different metallicities ($Z = 0.004$, $Z = 0.008$, and solar $Z = 0.02$), visual reddening ranging $0 < E(B-V)_{\rm stellar} < 0.7$ and exponentially declining and delayed star-formation histories (SFH) with nine different τ values from 0.1 to 30 Gyr.

We adopt a Chabrier (2003) IMF and Calzetti et al. (2000) extinction law, while the contribution of emission lines to the stellar templates is considered in the SED fitting by using an empirical relation between the UV light and the emission line fluxes, as described in Ilbert et al. (2009). The stellar masses for the entire sample of galaxies are presented in Table B.3. Typical 1σ uncertainties in M_* are $\sim$0.2 dex and are obtained from the median of the probability distribution function (PDF). Thus, they do not account for possible systematic error (e.g., IMF variations). Besides M_*, additional physical parameters derived from SED fitting used in this paper are the extinction-uncorrected rest-frame magnitudes calculated with the method of Ilbert et al. (2005) and, for a subset of galaxies, stellar extinction $E(B - V)_{\rm stellar}$ and star-formation rates (SFR$_{\rm SED}$).

4.2. Extinction correction

In order to derive extinction-corrected luminosities, we first obtain the logarithmic extinction at Hβ, c(Hβ), from the Balmer decrement. Using either Hα and Hβ lines or Hβ and Hγ when Hα is not available, we use the following formulation,

$$c(\mathrm{H}\beta)_1 = \log\left(\frac{\mathrm{H}\alpha/\mathrm{H}\beta}{2.82}\right)/f_{\mathrm{H}\alpha} \tag{1}$$

$$c(\mathrm{H}\beta)_2 = \log\left(\frac{\mathrm{H}\gamma/\mathrm{H}\beta}{0.47}\right)/f_{\mathrm{H}\gamma} \tag{2}$$

where the observed ratios are divided by the theoretical values (Hα/Hβ = 2.82 and Hγ/Hβ = 0.47) and for case B recombination with $T_{\rm e}$ = 2×10^4 K, $n_{\rm e}$ = 100 cm^{-3} following Amorín et al. (2015); $f_{\mathrm{H}\alpha}$ and $f_{\mathrm{H}\gamma}$ are the coefficients corresponding to the Cardelli et al. (1989) extinction curve at the wavelength of the Hα and Hγ emission lines ($f_{\mathrm{H}\alpha}$ = 0.313, $f_{\mathrm{H}\gamma}$ = 0.157), respectively.

For 111 galaxies in our sample, we only have one hydrogen line available or the Hα/Hβ and Hβ/Hγ ratios are below their theoretical values. In these cases, we derive the gas extinction from the stellar reddening, given by the SED fitting ($E(B - V)_{\rm stellar}$). The reddening of the stellar and nebular components of a galaxy are generally different, and various relations between the two have been found in previous studies. Calzetti et al. (2000) found that the gaseous reddening is typically higher than reddening in low-redshift starburst galaxies, which are more similar to our sample. They apply the following relation $E(B - V)_{\rm nebular} = E(B - V)_{\rm stellar}/0.44$. More recently, Reddy et al. (2010) found that choosing $E(B - V)_{\rm nebular} = E(B - V)_{\rm stellar}$ is more appropriate for studying $z \sim 2$ star-forming galaxies, while Wuyts et al. (2013) derived a relation for massive star-forming galaxies at $0.7 < z < 1.5$: $E(B-V)_{\rm gas} = E(B-V)_{\rm stellar} + E(B-V)_{\rm extra}$, where $E(B-V)_{\rm extra} = E(B-V)_{\rm stellar} \times (0.9 - 0.465 * E(B-V)_{\rm stellar})$. The
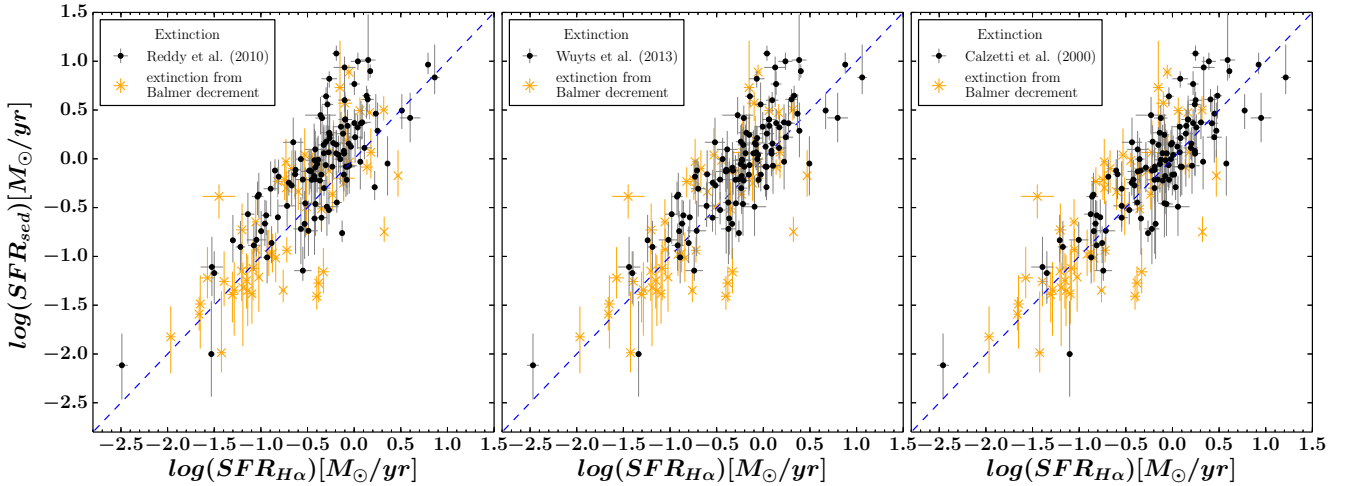
Fig. 5. Comparison between star-formation rates derived from SED fitting (SFR$_{SED}$) and from the extinction-corrected Hα luminosity (SFR$_{H\alpha}$), for different calculations of the extinction coefficient c(Hβ) for the galaxies without an available Balmer decrement. *From left to right*: $E(B-V)_{gas} = E(B-V)_{stellar}$ (Reddy et al. 2010); $E(B-V)_{gas} = E(B-V)_{stellar} + E(B-V)_{extra}$ (Wuyts et al. 2013); $E(B-V)_{gas} = E(B-V)_{stellar}/0.44$ (Calzetti et al. 2000). In the *last panel*, the orange crosses represent the galaxies with Balmer decrement available, for which the SFR$_{H\alpha}$ are consistent with the SFR$_{SED}$ and no systematic trend is observed.

latter result indicates that nebular light is more attenuated than the stellar light, but the extra-correction is lower than predicted by Calzetti et al. (2000).

In order to decide which relation between stellar and nebular reddening should be applied to our galaxies, we analyze all three possibilities listed above. We derive star-formation rates (SFR) from extinction-corrected Hα luminosities (SFR$_{H\alpha}$, see Sect. 4.3) and compare them with the SFR derived through SED fitting SFR$_{SED}$ (Fig. 5).

We find when using the relation by Reddy et al. (2010), the SFR$_{H\alpha}$ are systematically lower than the SFR$_{SED}$, and the differences increase toward higher SFRs where extinction corrections are more severe. Using the relations by Wuyts et al. (2013) and Calzetti et al. (2000), we find a tighter correlation and a better agreement between the two SFR measurements, with the latter having the lowest offset ($\simeq -0.08$ dex) in the whole range of SFR and the lowest dispersion ($\simeq 0.32$ dex). Repeating the same procedure for the galaxies with extinction derived through Balmer decrement, we see that despite the larger scatter, there is no systematic trend between SED and Hα-based SFRs, supporting the consistency of this method.

Overall, we decided to adopt the extinction derived through the Balmer decrement for those galaxies with at least two hydrogen lines available. For the remaining galaxies, we used the stellar reddening and the relation by Calzetti et al. (2000); then, following the same paper, we obtained the extinction coefficient c(Hβ) from the corrected reddening as:

$$c(H\beta)_3 = E(B-V) \times 0.69. \qquad (3)$$

The extinction from SED fitting is used for 109 galaxies in our sample.

4.3. Star-formation rates from Balmer lines

In order to derive the ongoing star-formation rate of the galaxies (i.e., the star-formation activity in the last 10–20 Myr), we adopt the standard calibration of Kennicutt (1998),

$$SFR = 7.9 \times 10^{-42} L(H\alpha) \text{ [erg s}^{-1}] \qquad (4)$$

where L(Hα) is the Hα luminosity, corrected for extinction as described in the previous section. However, for galaxies at $z \geq 0.42$,

Hα is no longer visible in our VIMOS spectra. To overcome this limitation, we estimate the Hα luminosities from Hβ fluxes by assuming the theoretical ratio (Hα/Hβ)$_0$ = 2.82, valid for case B recombination. Following Santini et al. (2009), the SFR derived this way have been scaled down by a factor of 1.7 in order to be consistent with the Chabrier (2003) IMF used throughout this paper.

We note that corrections for slit losses due to the finite size of the slit (1″) have already been applied to all the spectra during the calibration process, and it is as accurate as the observed-frame optical photometry. This allows us to efficiently compare photometric (e.g., stellar masses) and spectroscopic quantities (e.g., SFR$_{H\alpha}$, metallicity), which are investigated in the following sections. The consistency between Hα-based and SED-based SFRs, shown in Fig. 5, supports this procedure.

Finally, we combine Balmer line-based SFRs with stellar masses in order to compute the specific star-formation rate ($sSFR = SFR/M_*$).

4.4. Morphology and sizes

We perform a visual classification of our star-forming dwarf galaxies as a first approach studying their morphological properties. The selected galaxies are almost unresolved in ground-based CFHT images, but for most of them (those in COSMOS and ECDFS fields), space-based images are available, as presented in Sect. 2.2. In order to have a homogeneous sample, avoiding strong biases in the classification due to the much lower resolution of CFHT images, we analyze only the galaxies in COSMOS and ECDFS (101 in total). For this subset, we do the classification based on HST-ACS *F814W* band images.

Galaxies at higher reshifts typically show irregular shapes, therefore we cannot follow the Hubble morphological classification and instead need to choose ad-hoc criteria. In this paper, we divide our galaxy sample into the four morphological classes defined by Amorín et al. (2015) (A15) for low-mass EELGs (EW([O III])λ5007 $>$ 100 Å) in our identical redshift range, applying the criteria also to our non-EELGs. These include Round/Nucleated, Clumpy/Chain, Cometary/Tadpole and Merger/Interacting morphological types. A visual inspection
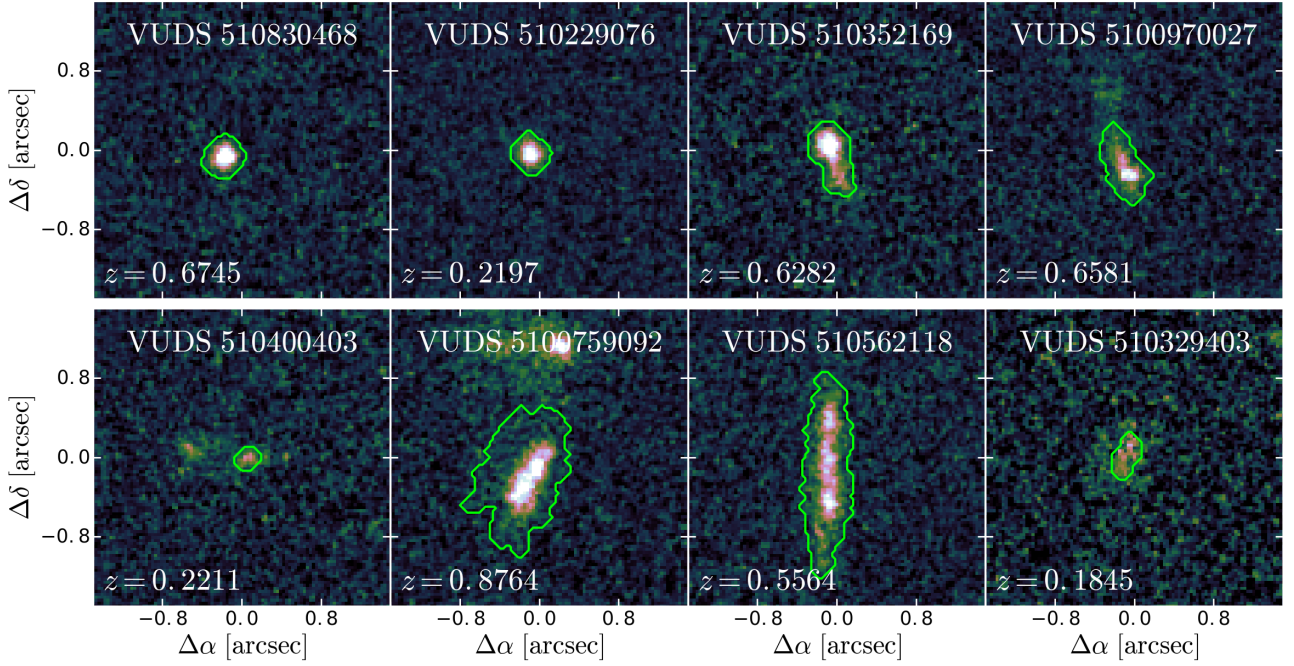
Fig. 6. HST i-band images of eight galaxies in the COSMOS field with different morphological properties. We have: (*top line*) two round-nucleated galaxies at different redshifts and two cometary-tadpole systems; (*bottom line*) two interacting-merging galaxies (a faint close galaxy pair and a brighter loose couple), a clumpy-chain system and finally an example of low-surface-brightness dwarf. The stamps are 2×2 arcsec wide and the green lines represent the contours of the galaxies.
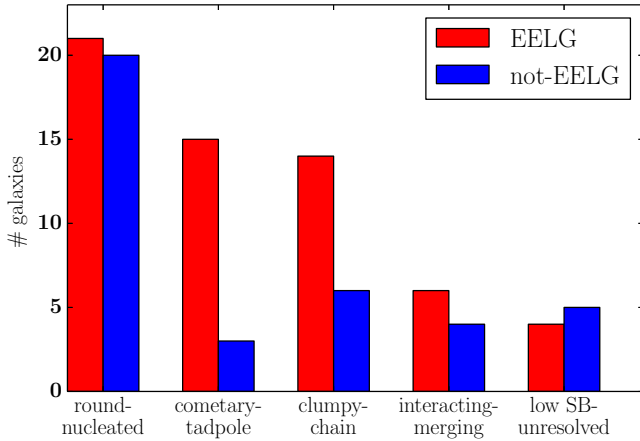
Fig. 7. Bar histogram showing the number of galaxies falling into each morphological class described in the text for EELG (red) and non-EELG (blue) subsamples. We find that EELGs have a higher fraction of irregular and disturbed morphologies (58%) compared to non-EELGs (34%). Only galaxies in COSMOS and ECDFS fields are considered for this analysis.

of our complete sample of galaxies in COSMOS and ECDFS fields reveals that, following the classification by A15, $\simeq40\%$ are round-nucleated, $\simeq20\%$ are clumpy-chain, $\simeq16\%$ are cometary-tadpole, and $\simeq10\%$ are merger-interacting systems, while for the remaining 14% fraction, we cannot determine their morphological type because they appear unresolved or have extremely low surface brightness. As an example, we show (Fig. 6) HST *F814W* images for each galaxy morphological type, while in Fig. 7, we show the distribution of the EELG subsets. Even though there might be inevitable overlap between the last three classes, the latter analysis shows qualitatively that EELGs have, on average, more disturbed morphologies (cometary, clumpy

shapes and interacting-merging systems) compared to non-EELGs, similarly to what was found in A15.

We obtain quantitative morphological parameters for the galaxies in our sample with HST-ACS images available. The analysis was performed using GALFIT (Peng et al. 2002, 2010, version 3.0), following the methodology presented in Ribeiro et al. (2016), based on recursively fitting a single two-dimensional (2D) Sérsic profile (Sérsic 1968) to the observed light profile of the object. Using this procedure, we obtained the effective radius (semi-major axis) $r_{\rm e}$ and the ratio between the observed major and minor axis of the galaxy, q.

We do not deproject $r_{\rm e}$ to avoid the introduction of additional uncertainties (given by q), thus we may underestimate the SFR surface density for the most elongated galaxies. However, given the large fraction of round and symmetric galaxies in our sample, we consider the effective radius to be good enough to characterize the size of the objects for our purposes. Furthermore, we assume that half of the total star-formation rate (derived from Hα luminosity) resides inside the effective radius. This approximation depends on the distribution of the gas relative to the stellar component and can have an opposite effect of deprojection.

Finally, some caveats should be considered when applying GALFIT to our sample. The minimization procedure of the code weighs more the central parts of the object, where the S/N is higher and the nebular emission lines along with young stellar populations contribute the most, inducing an underestimation of the true scale length of the underlying galaxy (Cairós et al. 2007; Amorín et al. 2007, 2009). However, SFDGs (e.g., Blue Compact Dwarfs) are usually dominated by nebular emission lines at all radii, and the gas is typically more extended than the central stellar body (Papaderos & Östlin 2012, e.g., IZw18), producing a compensation of the previous effect.

For the galaxies in the VVDS-02h field observed with CFHT, GALFIT does not reach a stable solution in most of the

cases (50%). Even when the fitting code converges, the effective radii suffer from systematic overestimation (difficult to quantify) due to the lower image resolution, as shown in previous VUDS works (Ribeiro et al. 2016). This effect can be especially important for our dwarf galaxies since they are intrinsically very small, as we illustrate in Sect. 5. For these reasons, for the quantitative analysis also, we only consider the galaxies in COSMOS and ECDFS.

4.4.1. Gas fractions and surface densities

We analytically derive SFR surface densities and stellar mass surface densities, dividing SFR and M^* by the projected area of the galaxy by assuming:

$$\Sigma_{\rm SFR} = \frac{SFR}{2\,\pi r_{\rm e}{}^2} \tag{5}$$

$$\Sigma_{M_*} = \frac{M_*}{2\,\pi r_{\rm e}{}^2}. \tag{6}$$

Gas surface density and total gas mass are then computed assuming that galaxies follow the Kennicutt-Schmidt (KS) law (Kennicutt & Evans 2012) in the form:

$$\Sigma_{\rm SFR} = (2.5 \pm 0.7) \times 10^{-4} \left(\frac{\Sigma_{\rm gas}}{1\,M_\odot\,{\rm pc}^{-2}}\right)^{1.4\pm0.15} M_\odot\,{\rm yr}^{-1}\,{\rm kpc}^{-2}. \tag{7}$$

Since this equation assumes a Salpeter IMF, here we have used SFRs consistent with this IMF. Inverting the above relation, we determine the gas surface density:

$$\Sigma_{\rm gas} = \left[0.4 \times 10^4 \times \left(\frac{\Sigma_{\rm SFR}}{1\,M_\odot\,{\rm yr}^{-1}\,{\rm kpc}^{-2}}\right)\right]^{0.714} M_\odot\,{\rm pc}^{-2}. \tag{8}$$

Then, multiplying again by the galaxy area, we derive the total baryonic mass of the gas involved in star formation:

$$M_{\rm gas} = \Sigma_{\rm gas} \times 2\,\pi(r_{\rm e})^2 \times 10^6\,M_\odot. \tag{9}$$

Finally, we derive the gas fractions as:

$$f_{\rm gas} = \frac{M_{\rm gas}}{M_{\rm gas} + M_*}. \tag{10}$$

In previous formulae, we have used Salpeter-based SFRs to be consistent with the expression of the KS law (derived assuming a Salpeter IMF). Likewise, the stellar masses M_* have been scaled to Salpeter IMF following Bolzonella et al. (2010) $(\log(M_*)_{\rm Salp} = 0.23 + \log(M_*)_{\rm Chab})$.

Some caveats should be considered when applying the KS law to our sample. Leroy et al. (2005) show that dwarf galaxies and large spirals exhibit the same relationship between molecular gas and star-formation rate, while Filho et al. (2016) find that the scatter around the KS law can be very large ($\sim$0.2–0.4 dex) depending on many galaxy properties (e.g., $f_{\rm gas}$, sSFR). In particular, extremely metal-poor (XMPs) dwarfs ($Z < 1/10\,Z_\odot$ Kunth & Östlin 2000) tend to fall below the KS relation, having unusually high HI content for their $\Sigma_{\rm SFR}$ and thus a lower star-formation efficiency. On the other hand, some dwarf galaxies with enhanced SFR per unit area appear to have higher ongoing star-formation efficiency (Amorín et al. 2016). The dispersion of the KS law, together with the less quantifiable uncertainty in the galaxy sizes, result in $f_{\rm gas}$ errors of at least 0.2–0.3 dex. Given that, the only way to have more reliable and constrained values of $f_{\rm gas}$ and $\Sigma_{\rm gas}$ would be to measure the gas content directly, such as using CO, dust or [CII] as H_2 mass tracers.

4.5. Derivation of chemical abundances and ionization parameter

In order to derive the metallicity and ionization parameter for the galaxies in our sample, we used the python code HII-CHI-mistry (HCm). For a detailed description about how this program works, we refer to the original paper by Pérez-Montero (2014) (PM14), and summarize here the basic principles.

4.5.1. $T_{\rm e}$−consistent, model-based abundances

HCm is based on the comparison between a set of observed line ratios and the predictions of photoionization models using CLOUDY (Ferland et al. 2013) and POPSTAR (Mollá et al. 2009). Compared to previous methodologies, the models consider all possible ranges of physical properties for our galaxies, including variations of the ionization parameter. This quantity is defined as:

$$\log(U) = \frac{Q(H)}{4\pi r^2 n c} \tag{11}$$

where $Q(H)$ is the number of ionizing photons ($\lambda < 912$ Å) in s^{-1}, r is the outer radius of the gas distribution in cm, c is the speed of light in cm/s, and n is the number density of hydrogen in cm^{-3}. The larger the value of $\log(U)$, the more ionized the gas, even though collisional ionization can play an important role, especially when the temperature of the gas is high (hundreds of thousands of degrees).

Assuming the typical conditions in gaseous ionized nebulae, the grid probes possible values of $\log(U)$ in the range $[-1.50, -4.00]$, metallicity $12 + \log({\rm O/H})$ in the range $[7.1, 9.1]$, and $\log({\rm N/O})$ between 0 and -2. Using a robust χ^2 minimization procedure, HCm allows the derivation of three quantities: the oxygen abundance (O/H), the nitrogen over oxygen abundance (N/O), and the ionization parameter ($\log(U)$), which best reproduce this set of five emission line ratios: [O II]$\lambda3727$ Å, [O III]$\lambda4363$ Å, [O III]$\lambda5007$ Å, [N II]$\lambda6584$ Å, and [S II]$\lambda\lambda6717 + 6731$ Å (all relative to Hβ), which are provided as input parameters. The procedure consists of two steps; in the first step a comparison is made between the observed extinction-corrected emission-line intensities and the grid of models, providing a value of N/O. Then, the nitrogen abundance is used to constrain the models and derive reliable oxygen abundance and ionization parameters with the same χ^2 minimization methodology.

HCm provides abundances that are consistent with those derived from the direct method for a large range of metallicity values and for a broad variety of galaxy types in the local Universe. The agreement between the model-based O/H and N/O abundances and those derived using the direct method is excellent when all the lines are used. Reliable model-based estimation of O/H can also be obtained without [O III]$\lambda4363$ Å detection if a limited grid of models is adopted using an empirical relation between $\log(U)$ and $12 + \log({\rm O/H})$. The relation between the metallicity and the ionization parameter arises from the physical properties of gaseous nebulae. It is consistent with large samples of local star-forming galaxies and HII regions (PM14), and has also been tested for the SFDGs in our sample with detected [O III]$\lambda4363$ Å lines, in which case no assumptions are made by the code. The role of this relation is to minimize the dispersion in the determination of O/H (PM14). Finally, when only [O II]$\lambda3727$ Å, [O III]$\lambda5007$ Å, and Hβ are observed (the code is assuming a typical ratio between [O III]$\lambda5007$ Å and [O III]$\lambda4959$ Å of 3.0, Osterbrock 1989),
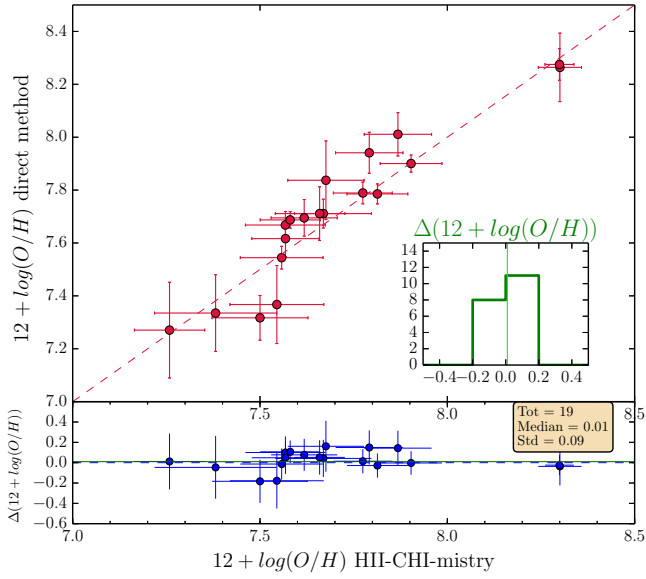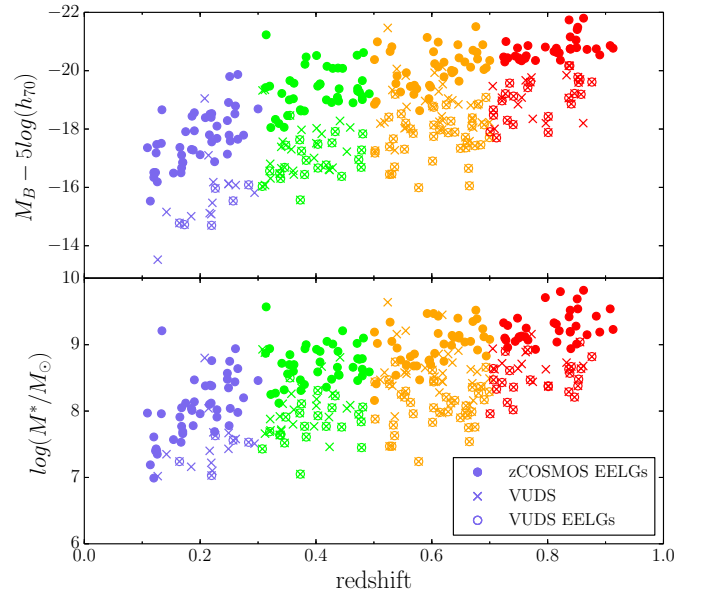
Fig. 8. Comparison between the metallicity derived with the code HCm and the direct method, showing the consistency of our approach. The red dashed line is the 1:1 relation. At the *bottom of the figure*, the differences between the two methods are plotted as a function of the metallicity. The blue dashed line corresponds to the 0 level, while the blue continuous line is the median value. In the *lower-right box*, we have added the histogram with the distribution of the differences, with the median value line in green.

Fig. 9. *Top*: $M_B - 5 \log h_{70}$ vs. redshift for our sample of galaxies (crosses) and for zCOSMOS EELGs by Amorín et al. (2015) (filled circles), color coded according to different bins of redshift (0.1–0.3, 0.3–0.5, 0.5–0.7 and 0.7–0.9). The EELG fraction of our galaxies is evidenced by empty circles around the crosses. The B-band luminosities span a wide range, $-13 \leq M_B \leq -21.5$, increasing with redshift. *Bottom*: Galaxy stellar mass vs. redshift for the same galaxy samples.

the $R23$ index ([O II]$\lambda3727$ Å + [O III]$\lambda\lambda4959 + 5007$ Å)/Hβ is used as a proxy to derive O/H, in combination with the [O II]$\lambda3727$ Å/[O III]$\lambda5007$ Å ratio to partially remove the dependence on $\log(U)$. This is the most frequent case for our sample, since 93% of our SFDGs without an auroral line detection also have no detected [N II]$\lambda6584$ and [S II]$\lambda\lambda6717, 6731$.

The procedure described above allows us to apply HCm for galaxies beyond the local Universe, where galaxies are fainter and [O III]$\lambda4363$ Å is generally not detected. HCm shows an increase of the dispersion (compared to the direct method) when a lower number of emission lines is considered, but gives results that are more consistent with the direct method than other empirical and theoretical calibrations. We find that the systematic differences with respect to HCm (and the direct method) can be as high as ∼0.7 dex at lower metallicities, depending on the adopted calibration. We refer to Appendix A for a description of the calibrations analyzed in this paper and a more detailed comparison with our results.

4.5.2. Direct method

For a fraction of galaxies in our sample (19), we detect the [O III] $\lambda4363$ Å auroral line, which is sensitive to the electron temperature T_e. This allows us to use the direct method and check the consistency with metallicities for these galaxies derived through HCm. Despite the small number of galaxies, the two methods give consistent results within the errors over the entire metallicity range for the majority of them (Fig. 8). We do not find any systematic trend in the low- or high-Z regime, and the median difference between the two measurements is of 0.01 dex. According to PM14, the consistency between HCm and the direct method, tested for an analogous sample of local star-forming galaxies, is of ∼0.15 dex. In our case, the 1σ scatter is of the same order of magnitude (∼0.09 dex); even lower

than the previous value. Thus, we safely apply the code HCm to the other galaxies in the sample without auroral line detection.

5. Results

In this section, we present the properties of the SFDG sample and we study the key scaling relations between them. The main physical quantities presented here are listed in Table B.3.

In Fig. 9, we show that the stellar masses of the galaxies, derived through SED fitting, span a wide range of values from 10^{10} down to $10^7 M_\odot$ (median value of $10^{8.2} M_\odot$), a region in the stellar mass distribution of galaxies which is still strongly under-represented in current spectroscopic surveys at intermediate redshift. Compared to zCOSMOS EELGs (A15), which is one of the largest samples of low-mass star-forming galaxies at these redshifts (see also Ly et al. 2016b), we extend the intrinsic luminosity of the sources (given in rest-frame absolute magnitude M_B) down by ∼2 mag thanks to VUDS deeper observations. As a consequence, our sample extends to lower stellar masses, though we are biased toward the higher M_* at a given redshift.

In Fig. 10, we present the distribution of various physical quantities: extinction correction $c(\text{H}\beta)$, specific star-formation rate (sSFR), effective radius (r_e), gas fraction (f_{gas}), ionization parameter ($\log(U)$) and oxygen abundance ($12 + \log\text{O/H}$). The histogram of extinction coefficients shows that the dust extinction is generally low, with median reddening of $E(B - V) = 0.45$ mag ($\sigma = 0.38$), and there is no significant difference between EELG and non-EELG distributions. The reddening values found here are consistent with previous studies on local (e.g., Kniazev 2004) and intermediate-redshift samples of SFDGs (e.g., Amorín et al. 2015; Ly et al. 2014, 2015). Our galaxies have low to moderate SFRs ranging $10^{-3} \lesssim SFR \lesssim 10^1 M_\odot$ yr^{-1}, with a median $SFR = 0.64 M_\odot$ yr^{-1}, and 1σ scatter of 0.6. As a consequence, the sSFR tend to be high, spanning a broad range, 10^{-10} yr$^{-1} \lesssim sSFR \lesssim 10^{-7}$ yr^{-1}, with a tail of very high
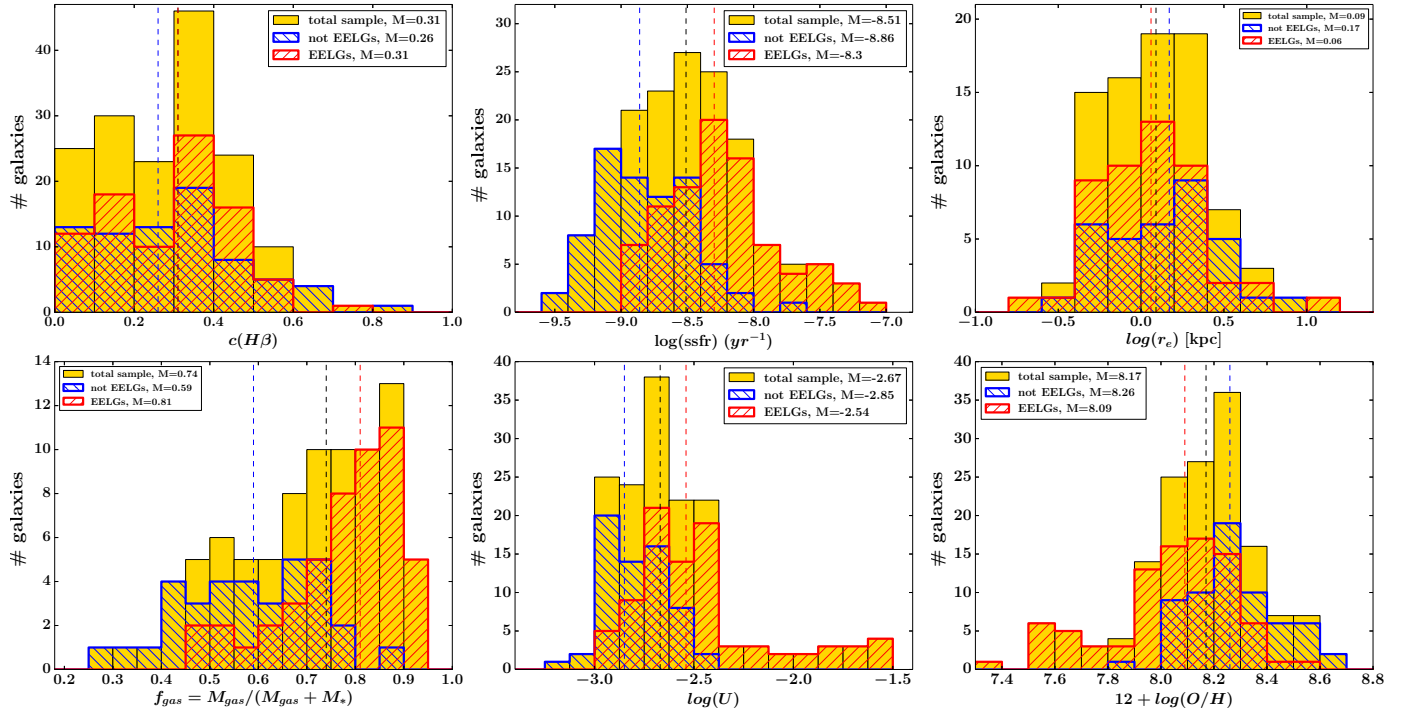
Fig. 10. Histogram distribution of extinction coefficient $c(H\beta)$, sSFR, and circularized effective radius r_e *(top)*, gas fraction f_{gas}, gas-phase metallicity and ionization parameter $\log(U)$ *(bottom)* for our selected galaxies. The EELG and non-EELG fractions are highlighted with red and blue lines, respectively, filling the histogram. The median distribution values for each quantity are indicated in the legend for each subset of galaxies.

sSFR galaxies. The whole sample has a median of 10^{-9} yr^{-1}, well above the Milky Way integrated sSFR ($\sim 1.5 \times 10^{-11}$ yr^{-1}).

We also find that our galaxies are very compact, with effective radii (in kpc) in the range $0.1 \leq r_e \leq 6$ kpc and median value of $r_e = 1.2$ kpc (standard deviation of 2.3 kpc), comparable to BCDs (Papaderos et al. 1996; Gil de Paz & Madore 2005; Amorín et al. 2009) and the Green Pea galaxies (Amorín et al. 2012). In the same figure, we show the distribution of values of the gas fraction of our SFDGs. The values range $0.25 < f_{gas} < 0.95$, and the distribution is peaked toward higher f_{gas}, with one half of our galaxies showing $f_{gas} > 0.74$, that is, more than 74% of the total baryonic mass resides in their gas reservoirs. The highest values are found in EELGs, which show a median $f_{gas} \sim 0.2$ higher compared to non-EELGs. These results for the whole sample could be an indication that the star-formation efficiency has been very low or that our galaxies are very young and still assembling most of their stellar mass. In the local Universe, such values of gas fractions can be found in low-mass, low-metallicity and highly star-forming galaxies (e.g., Lara-López et al. 2013; Filho et al. 2016; Amorín et al. 2016).

5.1. The relation between star-formation rate and stellar mass

For high-mass star-forming galaxies ($M_* > 10^9 \, M_\odot$), a tight correlation has been found between the star-formation rate and the stellar mass (e.g., Brinchmann et al. 2004; Elbaz et al. 2007; Tasca et al. 2015) up to redshift 5. This correlation, called the star-formation main sequence (MS), is displaced toward higher values of SFR at higher z, with an almost constant slope of approximately 1 (Guo et al. 2015) and a small non-varying SFR dispersion of ~ 0.3 dex (Schreiber et al. 2015). An extension of the MS has been derived by Whitaker et al. (2014) for intermediate-redshift star-forming galaxies ($0.5 < z < 1$) down

to $M_* \sim 10^8 \, M_\odot$, but the relation remains poorly constrained at lower masses.

Our sample of 164 VUDS SFDGs allows us to populate the low-mass end of the SFR-M_* relation (Fig. 11). Our sample has a higher average SFR per unit mass compared to the extrapolation of the MS at low masses ($M_* < 10^{8.4} \, M_\odot$, Whitaker et al. 2014) This result should be considered as a secondary effect of our selection criteria, based on a $S/N > 3$ cut on hydrogen recombination lines, [O II]λ3727 and [O III]λ5007 (see Sect. 3.1). At a given continuum luminosity and stellar mass, we are limited to the brighter Hα (Hβ) values (i.e., higher sSFRs) compared to a continuum S/N-selected sample. We also notice that a conspicuous number of SFDGs have higher star-formation rates than the median population, with starburstiness parameters (defined as SFR/SFR$_{MS}$, Schreiber et al. 2015) up to 1.8 dex, similar to zCOSMOS EELGs.

This difference is more evident when we consider the sSFR versus M_*. The sSFR distribution of the EELG fraction is biased high ($\sim+0.6$ dex) with respect to the non-EELGs. We also find that the starburstiness parameter depends on the gas fraction. In particular, the median gas fraction of the sample ($f_{gas;med} = 0.74$) is very effective for distinguishing between these two classes, with more gas-rich galaxies having, on average, higher sSFRs (~ 1 dex) compared to the MS star-forming population (Fig. 12).

### 5.2. Chemical abundances and ionization properties

In the last two panels of Fig. 10, we present the results of the code HCm, the ionization parameter, and the metallicity. We discard, from this analysis, 10 galaxies of our VUDS original sample for which some of the emission lines required by the code are not reliably detected. For the remaining 152 galaxies, we find that they span a wide range of values, respectively $-3.17 < \log(U) < -1.55$ and $7.26 < 12 + \log(O/H) < 8.6$.
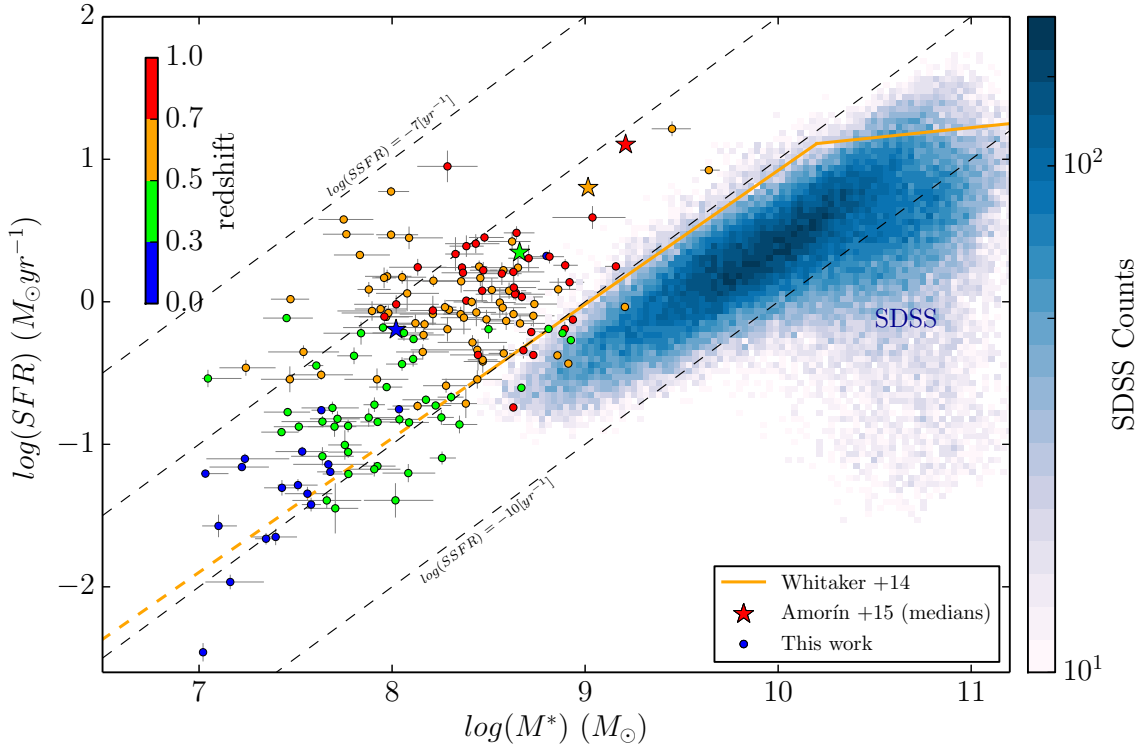
Fig. 11. Diagram of SFR vs. M_* for our sample. The galaxies are coded with different colors according to four redshift bins, and the colored stars represent the medians for zCOSMOS galaxies (Amorín et al. 2015) in four bins of masses. The orange continuous line represents the star-forming galaxies at similar redshift $0.5 < z < 1$ (the so-called "Main Sequence of Star Formation") derived by Whitaker et al. (2014). We extrapolate this line to the low-mass end of the diagram (dashed line). The dashed gray lines correspond to constant SSFR values, going from 10^{-10} yr^{-1} to 10^{-7} yr^{-1}. We show our SDSS sample described in Sect. 2.3 using a blue 2D histogram.
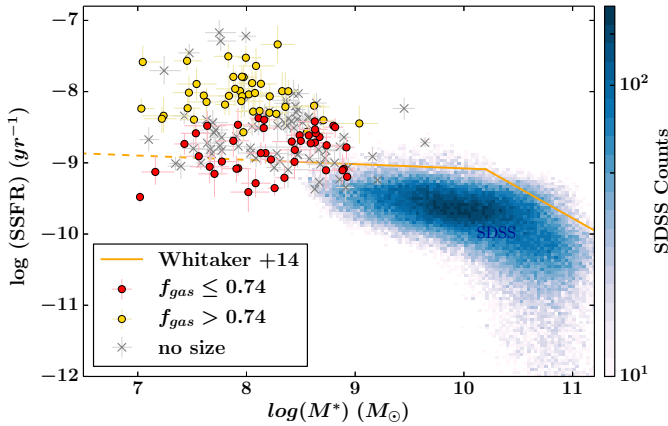

Fig. 12. Diagram of sSFR vs. M_* for our galaxies, coded by f_{gas} (below). The segregation is evident between galaxies with higher and lower gas fraction than the median $f_{gas,med} = 0.74$. The EELG fraction is evidenced with yellow colored circles.
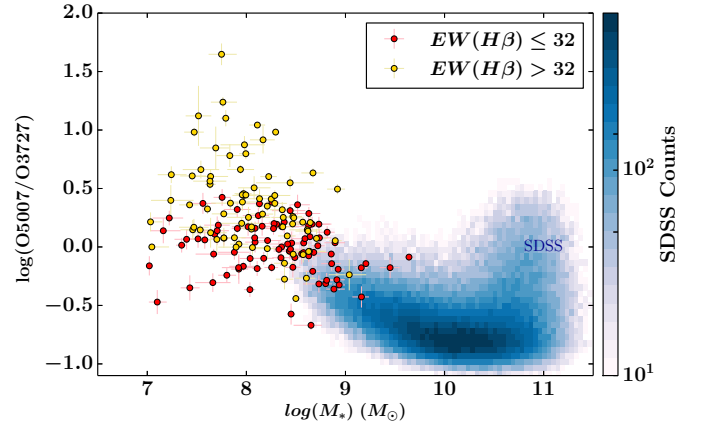
Fig. 13. Comparison between extinction corrected [O III]/[O II] and stellar mass M_* for our sample of galaxies, extending the diagram of local star-forming galaxies (blue 2D histogram) to lower masses. A color-coding is adopted according to EW(Hβ) higher or lower than the sample median (32 Å).

The ionization parameter distribution has median value $\log(U)_{med} \simeq -2.6$, with an extended tail of objects toward higher ionizations. In Fig. 13, we see that high ionization is found preferentially in lower-mass objects. In this plot, we compare the stellar mass to the extinction corrected emission line ratio [O III]$\lambda5007$/[O II]$\lambda3727$, which is typically used as a proxy of the ionization parameter and is the most common ionization parameter diagnostic (Baldwin et al. 1981). Our SFDGs show a broad variety of conditions ranging $-0.5 <$ [O III]$\lambda5007$/[O II]$\lambda3727 < 1.3$, and a mild correlation is found with M_*; though the scatter increases largely at lower

masses. Compared to the bulk of local star-forming galaxies (SDSS), VUDS SFDGs show, on average, higher ionizations, reaching $\log$([O III]$\lambda5007$/[O II]$\lambda3727$) ~ 1, which makes them more similar to the typical ionization conditions found at higher redshifts (Nakajima & Ouchi 2014). As we discuss later, this type of object is important for understanding the properties of faint star-forming galaxies in re-ionizing the Universe at $z > 6$. In particular, high ionization parameters traced by [O III]$\lambda5007$/[O II]$\lambda3727$ may indicate the presence of
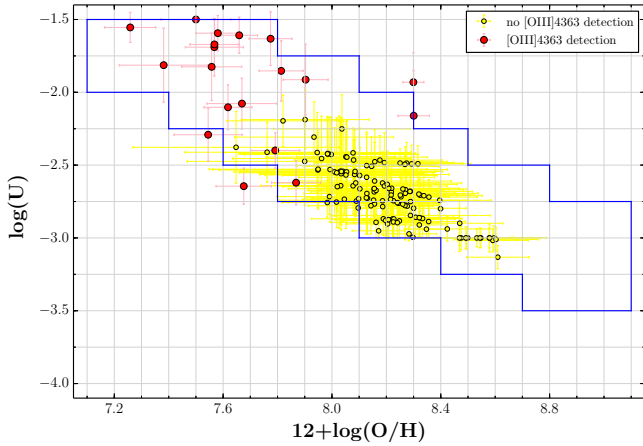
Fig. 14. Comparison between the metallicity $12 + \log(O/H)$ and $\log(U)$, both derived with the code HCm. The plot shows the anti-correlation between the two quantities, with the limited grid of models (green continuous line) considered by HCm when only [O III]3727 Å and [O III]5007 Å are available. Red points are the galaxies in our sample [O III]4363 detection, showing that the empirical relation is real, since HCm does not introduce any assumptions in this case.

density-bound HII regions, that is, those escaping LyC radiation (e.g., Jaskot & Oey 2013).

In the metallicity distribution histogram, we see that all the galaxies in our sample have sub-solar oxygen abundances, that is, $12 + \log(O/H) < 8.69$, and the median is 8.17, consistent with zCOSMOS EELGs, which have a median value of 8.16.

In Fig. 14, we compare for our galaxies the metallicity and the ionization parameter for our galaxies, both outputs of HCm. When the auroral line [O III]λ4363 Å is not detected, HCm considers a limited grid of models, which account for the anti-correlation between metallicity and ionization observed in local star-forming galaxies and giant HII regions, which originate in the physical properties of the nebulae. Enclosed by a blue solid line, we show the grid of models that we have used and the relation for our [O III]4363-detected galaxies, for which no assumptions are made on the relation $12 + \log(O/H)$ vs. $\log(U)$ by HCm. Instead, we apply this constraint to the rest of the sample where an auroral line is not detected, to minimize the dispersion in the determination of metallicity.

Finally, we notice that 12 galaxies in the sample are highly metal deficient and lie in the category known to as XMP galaxies ($Z < 1/10~Z_\odot$ Kunth & Östlin 2000). One galaxy has a metallicity of 7.26 ± 0.1 (VUDS J100045.13+022756.0), which is below 1/20 solar (<7.4); its value is comparable to the most metal-poor galaxies known (e.g., I Zw 18, Izotov & Thuan 1999). In this subset of XMPs, 11 have detection of the [O III]4363 line.

5.3. The mass-metallicity relation

In this section, we study the low-mass end of the MZR of SFGs, which can provide valuable insight into the physical processes regulating the mass assembly and chemical evolution of low-mass galaxies.

Even though the MZR has been well-determined at higher masses ($M_* > 10^9~M_\odot$) (Tremonti et al. 2004), it is still not completely defined at lower masses, where it has been studied in the local Universe by Lee et al. (2006), Zahid et al. (2012b), and Andrews & Martini (2013), but tested at intermediate redshift

($z < 1$) with relatively small samples (e.g., Henry et al. 2013; Ly et al. 2014, 2015, 2016b).

In Fig. 15, we present the mass-metallicity diagram for our sample of SFDGs, which provides new observational constrains to its low-mass regime. Our objects populate a large region at lower masses compared to the bulk of local star-forming galaxies, while the dispersion is high and appears to increase from solar to strongly subsolar values. Despite the large overall scatter, we find some agreement with the local MZR derived by AM13. In particular, 50% of our galaxies follow the local T_e-based MZR of AM13 to within their $\pm 1\sigma$ uncertainty ($\simeq 0.2$ dex), while a large number ($\sim$40%) are located below the 1σ limit. For individual galaxies, we find a maximum difference with the metallicity that corresponds to AM13 MZR at a given mass of $\sim$0.9 dex.

In order to characterize the MZR for our SFDGs, we divide the sample into four bins according to their stellar mass in order to have approximately the same number of galaxies in each bin (intervals of $\log(M_*)$ are: 7.0–7.5, 7.5–8.0, 8.0–8.5 and 8.5–9.5). For those falling into the same bin, we compute the weighted mean metallicity and 1σ standard deviations (std). Finally, we connect the mean points with a continuous line and the 1σ limits with dashed lines. The slope of our MZR is lower compared to the local relation of AM13, while it is better in agreement with the MZR found by Lee et al. (2006) using 27 nearby SFDGs with good measurements of T_e (with a small offset toward higher metallicities). We also find that the overall dispersion of our MZR (computed as the average 1σ-std of the metallicities in the four bins) is of $\sim$0.26, though it increases by 0.1 dex towards very low masses, reaching 0.34 in the last mass bin. The exact values of the mean metallicity and std for each bin are reported in the legend of Fig. 15.

Finally, in order to check for a possible dependence of our results on the S/N used to select our sample (Sect. 3.1), we tested three different S/N lower-limits (3–5) on the following emission lines critical for the determination of metallicity: [O II]λ3727 Å, [O III]λ5007 Å, and Hβ. Choosing a higher S/N threshold, applied simultaneously to the three above emission lines, reduces the total number of galaxies in the sample (from 164 to 111 for $S/N = 5$), but does not change our results. The average metallicities in the four bins scatter by less than 0.04 dex ($\sim$5%), which is lower than the mean uncertainty of the metallicity estimations. Likewise, the overall slope and 1σ deviation remain consistent with our former result.

5.4. The dependence of the metallicity on the stellar mass and SFR

Now, we investigate the relation between the metallicity and the specific SFR proposed by (Lara-López et al. 2013), which appears to be modulated by the gas fraction.

Another scaling relation has been found for local star-forming galaxies relating the metallicity and the sSFR of the galaxies, with a dependence also on the gas fraction (Lara-López et al. 2013). For high-mass galaxies, this relation has been interpreted as an indication of evolution: galaxies evolve toward lower sSFRs and lower gas fractions as they form stars, increasing their metallicity at the same time because of the gradual chemical enrichment of their ISM by supernova explosions and stellar winds. Following this idea, in Fig. 16, we compare metallicity and sSFR for our sample of SFDGs, dividing the sample into four bins of f_{gas}. We see that the two quantities are still correlated in the low-metallicity regime, with $12 + \log(O/H)$ decreasing toward higher sSFR, even though the
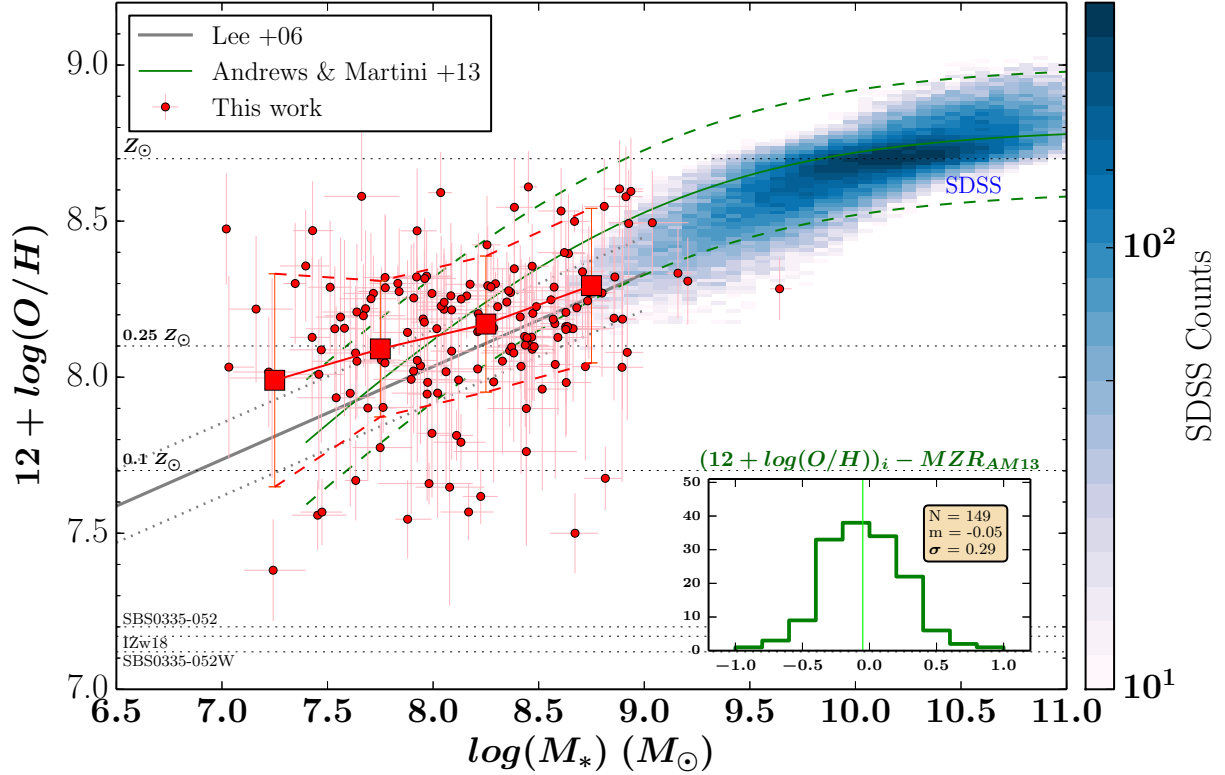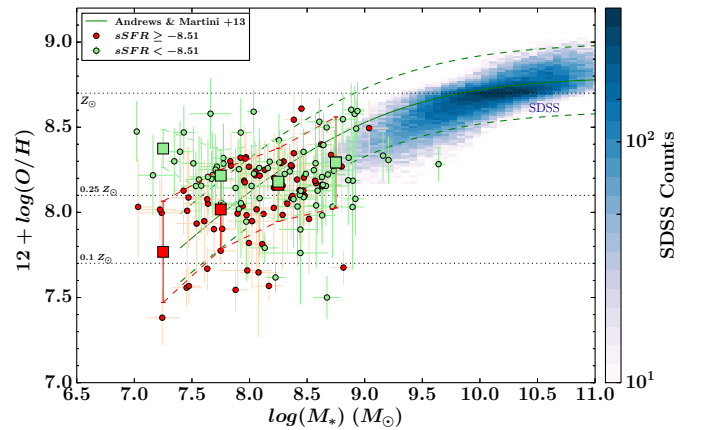
Fig. 15. Mass-metallicity diagram for our sample of galaxies, compared to the MZR of Andrews & Martini (2013) and Lee et al. (2006). The green dashed lines and grey dotted lines represent, respectively, the $\pm 1\sigma$ uncertainty of AM13 MZR ($\simeq 0.2$ dex) and the dispersion of L06 MZR ($\simeq 0.1$ dex). The horizontal dashed lines represent constant metallicities, referred to the Sun, and the levels of the three most metal poor galaxies known in the local Universe. We show in this figure also our error-weighted mean metallicities (red squares) and 1σ standard deviations calculated in four bins of mass ($\log(M_\odot) = [7–7.5, 7.5–8, 8–8.5, 8.5–9.5]$). The histogram in the inset shows the differences between the metallicities derived with HCm and those obtained from AM13 MZR at given stellar mass. Our sample is on average slightly below the AM13 relation (median difference of 0.05 dex), with a 1σ scatter around the median difference of 0.29 dex. We report here the mean and the 1σ-std for each of the four mass bins of our MZR, in increasing order of mass: ($m = 7.99$, $1\sigma = 0.34$), ($m = 8.06$, $1\sigma = 0.22$), ($m = 8.16$, $1\sigma = 0.22$), ($m = 8.29$, $1\sigma = 0.24$). The SDSS galaxy sample is shown with a blue 2D histogram.
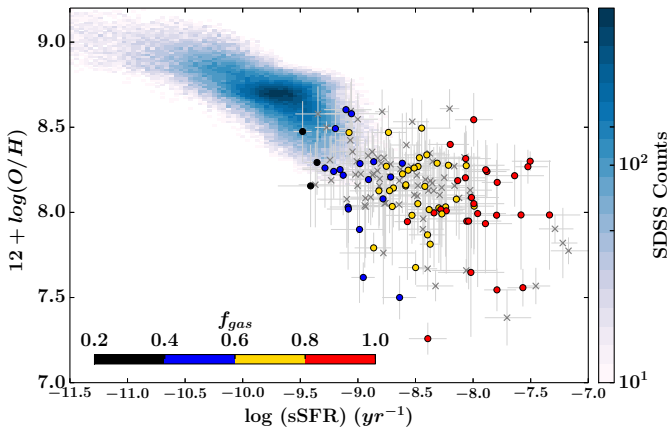
Fig. 16. Diagram of metallicity vs. sSFR for VUDS SFDGs. Different colors represent galaxies with different gas fractions, divided into four bins in f_{gas}: 0.2–0.4, 0.4–0.6, 0.6–0.8, and 0.8–1. Higher SSFRs also indicate higher gas fractions. Our sample extends the trend of local star-forming galaxies (the blue histogram) toward lower metallicities, showing that the SSFR is anti-correlated with the oxygen abundance, though the dispersion increases at higher sSFR. The overall scatter of the relation is ~0.5 dex in sSFR.

scatter is large. It is also evident that f_{gas} increases, on average, with sSFR (Fig. 16). We remind the reader that, given our definition of the gas fraction in Eq. (10), f_{gas} and the sSFR are not

Fig. 17. Mass-metallicity diagram for our galaxies, coded by the sSFR. We see that more metal-poor galaxies have, on average, higher sSFRs compared to those with higher oxygen abundances, and they follow different trends. The green dashed lines are $\pm 1\sigma$ uncertainty of AM13 MZR as in Fig. 15.

independent quantities (i.e., f_{gas} can be written as $1/(1 + k \times SFR/M_*)$, with k a constant factor), so this result is, in part, expected.

The scaling relation between metallicity and sSFR suggests that part of the scatter of our galaxies in the MZR can be

explained by assuming, at fixed mass, a dependence of 12 + log(O/H) on the sSFR. In Fig. 17, we divide our sample into two subsets using the median distribution value $sSFR_{med} = 10^{-8.51}$ yr^{-1}. We see that the dependence of our MZR on the sSFR gives two different results at M_* higher and lower than 10^8 $M_\odot$. The MZRs of the two subsets are well separated in the lower-mass part, with a mean metallicity offset of 0.5 dex, which is similar to the result found at $M_* > 10^{8.5}$ $M_\odot$ by Ellison et al. (2008) in the local Universe. On the contrary, they become very close at higher masses, suggesting that the MZR is independent from the sSFR, which is more in agreement with the results of Hughes et al. (2013) and Sánchez et al. (2013).

A similar result is seen for the gas fraction, as expected from the dependence between sSFR and f_{gas} in Fig. 16. Using the median population value ($f_{gas,med} = 0.74$), we have found that at $M_* < 10^8$ galaxies with higher f_{gas} are more metal-poor; but this distinction vanishes at higher stellar masses. Even though the dependence of the MZR on the gas content is unknown at low masses, a dependence of the MZR on the observed f_{gas} (similar to our finding at $M_* < 10^8$ $M_\odot$) has been observed by Bothwell et al. (2013) for SDSS star-forming galaxies in the high-mass regime ($M_* > 10^9$ $M_\odot$).

We remind the reader that, as explained in Sect. 5.1, we may miss a significant fraction of galaxies with very low levels of SFRs at the given stellar mass range. Our results indicate as well that at the lowest stellar masses ($M_* < 10^8$ $M_\odot$), where our dispersion is larger, galaxies with lower star-formation activity and gas fraction tend to have higher metallicity. Galaxies with similar properties or even more extreme properties (i.e., less star-forming and more metal-rich) have also been identified in the local Universe (Peeples et al. 2008) and interpreted as a connection with more evolved classes of dwarfs (Zahid et al. 2012a). Overall, the different trends observed at lower masses may be due to the increasing role of an underlying population of metal-rich low-mass galaxies, which broaden the scatter of the relation toward lower stellar masses, as found in some previous works (Zahid et al. 2012a).

5.5. Comparison with the FMR

In order to study the dependence of the MZR on the SFR, previous works by Mannucci et al. (2010) and Lara-López et al. (2010) have proposed the Fundamental Metallicity Relation (FMR), which is a three-dimensional (3D) relation in the space parameter defined by M_*, 12 + log(O/H) and SFR. It has been found that a particular 2D projection of the FMR (i.e., plotting the metallicity against the new parameter $\mu_\alpha = \log(M_*) - \alpha \log(SFR)$, with $\alpha \neq 0$) minimizes the scatter of the points compared to the MZR for a particular value of α (which corresponds to $\alpha = 0$). An extension of the FMR to low masses ($\lesssim 10^9$ $M_\odot$) has been presented by Mannucci et al. (2011).

Given that our sample is not complete in mass (due to the VUDS limiting magnitude, see Sect. 5) and SFR (as we have shown above in Sect. 5.1, due to the selection criteria in Sect. 3.1), our goal is not to derive a new relation representative of low-mass galaxies ($M_* < 10^9$ $M_\odot$). However, we compare our results with the FMRs found in previous studies using different values of the parameter α. In the first panel of Fig. 18, we show the comparison with the FMR of Andrews & Martini (2013) (AM13), who find $\alpha = 0.66$ using the direct method on M_*-SFR stacks for local star-forming galaxies and down to $\mu_{0.66} \simeq 7.5$. In the second panel of Fig. 18, we compare with the extrapolation to low-masses of the FMR by Mannucci et al. (2011)
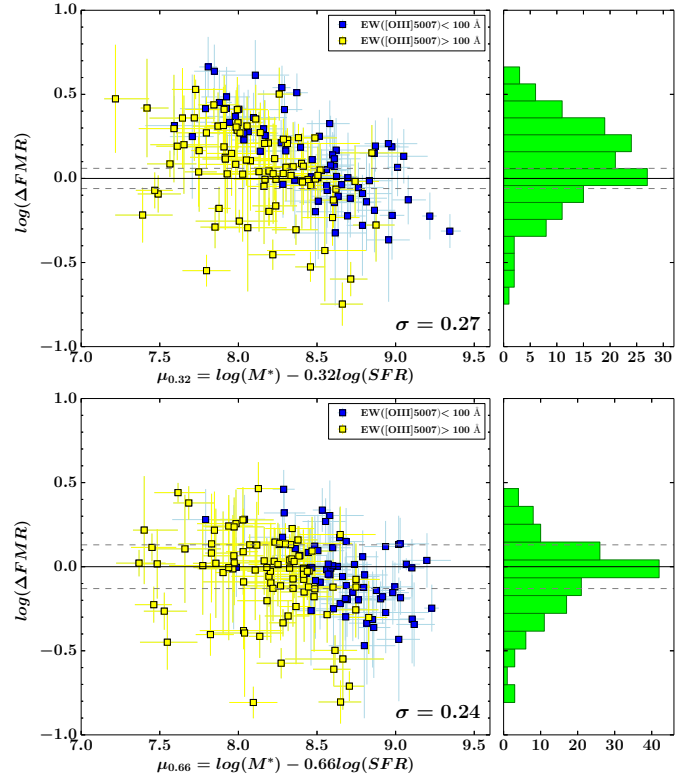

Fig. 18. Diagrams showing the differences between the HCm metallicities and the FMR of Mannucci et al. (2011) (*upper panel*) and Andrews & Martini (2013) (*bottom panel*). The dashed lines represent 1σ deviations for these relations. The EELGs in our sample ($EW([O\,III]5007) > 100$ Å) show slightly larger scatter in the FMR than the whole population, in agreement with Amorín et al. (2014).

(M11), calibrated in the low-Z regime ($\lesssim 8.4$) using objects with metallicities obtained through the direct method (Maiolino et al. 2008). The SFRs in both diagrams have been homogenized to the Chabrier (2003) IMF.

We find that, even though the position of our SFDGs is generally consistent with both the FMRs (as seen from the peak of the metallicity difference Δ(FMR) distribution), the scatter is larger than reported in the two previous studies. The 1σ standard deviations of our galaxies from AM13 and M11 FMRs are of 0.24 and 0.27 dex, respectively, and are higher than the median error on metallicity measurements from HCm. An increased dispersion with respect to the FMR has been shown for highly star-forming galaxies by Amorín et al. (2014), and could be due to differences in the methods for metallicity derivation or interpreted as an effect of the large spread of star-formation histories and current SFR in the low-mass range (e.g., Zhao et al. 2010).

5.6. MZR of galaxies with O4363 detection

In Fig. 19, we display the MZR of 22 galaxies in the VUDS sample for which the auroral line [O III]λ4363 has been detected. This subset is consistent in the low-mass range ($10^7 < M_* < 10^{8.5}$) with the sample of [O III]λ4363 selected galaxies compiled by Ly et al. (2014, 2015, 2016b). From this plot, we see that VUDS SFDGs with auroral line detection have lower metallicities at fixed mass compared to the median sample. Indeed, Telford et al. (2016) show that, at constant M_*, metal-poor galaxies have higher S/N of the oxygen lines in their optical spectra, particularly the auroral line, improving its detection. Therefore,
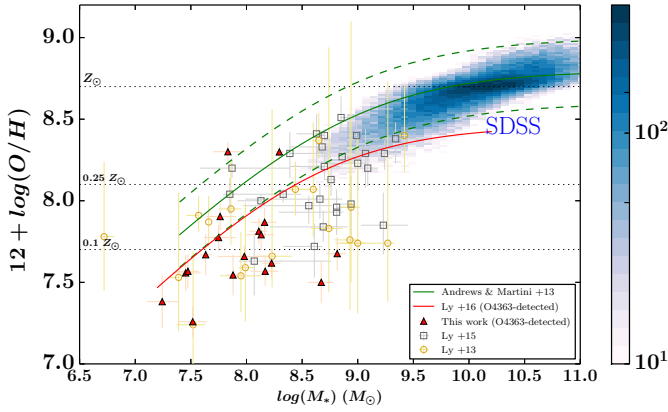
Fig. 19. Mass-metallicity diagram for the galaxies in our sample with [O III]λ4363 Å detection (red triangles), compared to the [O III]λ4363 galaxies with T_e oxygen abundances compiled by Ly et al. (2014, 2015) (open circles and open squares, respectively). The AM13 MZR and $\pm1\sigma$ uncertainty are shown with green lines. The red line indicates the best-fit MZR from Ly et al. (2016b) for galaxies with [O III]λ4363 detections.

our selection based on [O III]4363 tends to include those objects with the lowest metallicities in VUDS; they should have higher [O III]λ4363/[O III]λ5007 ratios, and the auroral line may be detected easier.

Finally, we studied the average sSFRs of the galaxies with [O III]λ4363 detection and, among them, the mean value of XMPs. We find that they are higher than the whole population of SFDGs ($sSFR_{mean} = 10^{-8.5}$) by 0.5 and 0.4 dex (respectively).

5.7. Comparison with the MZR of similar SFDGs samples

Recently, Ly et al. (2016b) (LY16) studied the mass-metallicity relation at low-mass and intermediate redshift with a sample of 164 emission-line galaxies (uniformly distributed in $0.1 < z < 1$) and abundances derived using the direct method for a subset of them (66) with [O III]λ4363 Å 3σ detection. Likewise, zCOSMOS EELGs compiled by A15 represent a very complementary sample to compare with, since their spectra are taken with the same instrument, they span the same z range, and they have similar properties to our galaxies, in particular to the EELG fraction. Here we recalculate the metallicity of these two datasets with our code HCm using the emission line fluxes retrieved from their catalog. Overall, we find a consistency between HCm metallicities and the A15 values.

In Fig. 20, we present the MZR including our SFDGs and the other two comparison samples. We see that the distribution of A15 galaxies is mainly consistent with VUDS SFDGs, though they are more massive, as we have shown before. At lower masses ($<10^{8.4}$ $M_\odot$), they are in agreement with the dispersion obtained for the VUDS galaxies, while at higher masses, a significant fraction of them are below our relation because the sample is biased towards more extreme objects. We notice in the same figure that the galaxies studied by LY16 are more consistent with the slope of the MZR found by AM13 than with ours. The differences with respect to our MZR may be due to the bias towards [O III]λ4363-detected galaxies in the LY16 sample, and this suggestion is also supported also by Fig. 19, as we have discussed before.

We also compare in Fig. 20 with the MZR found in the low-mass range ($10^8 < M_*/M_\odot < 10^9$) by Guo et al. (2016a) (G16), which is based on a large sample of 237 galaxies at intermediate

redshift ($0.5 < z < 0.7$) with 3σ [O III]λ5007 and Hβ detection. They estimate the metallicity from [O III]λ5007/Hβ line ratio and the calibration of Maiolino et al. (2008), using [O III]λ5007/[O II]λ3727 to break the lower- and upper-branch degeneracy. Compared to our study, their selection criteria are similar, but they do not require the detection of the [O III]λ4363 auroral line. Even though they determine the metallicity using a different method from that adopted in this paper, their MZR, extrapolated from 10^8 down to 10^7 $M_\odot$, is overall consistent with our result. In the lower mass bin the two mean metallicities coincide, and, in the whole mass range, the slope of their MZR is flatter than AM13 and more consistent with our relation. In the last three bins at higher masses there is a slightly increasing separation between the two means (up to 0.15 dex), which is likely due to the use of different metallicity estimators. Finally, the presence of an increasing scatter of the MZR toward lower masses reported in G16 is in agreement with our results. In particular, they obtain a scatter of ~0.3 dex at 10^8 $M_\odot$, which is the same as in our least massive bin. Their best-fit MZR (and 1σ uncertainties) is included in Fig. 20.

6. Discussion

6.1. Implications for galaxy assembly and evolution

The information on metallicity and gas fraction f_{gas} can be used to constrain chemical evolution models when applied to low-mass galaxies. In this paper, we use simple models of chemical evolution in order to investigate, from a broad point of view, the mechanisms that influence the ISM abundances of our SFDGs. We consider the closed-box model, in which galaxies do not interact with their environment, and two open-box models in which gas flows are allowed to flow in and out of a galaxy. In these models, the gas is well mixed at any time of the galaxy evolution (instantaneous mixing approximation) and newly born stars with $M_* > 1$ $M_\odot$ die and produce a stellar wind almost immediately (instantaneous recycling approximation). Gas outflows and inflows are assumed to occur at a constant fraction of the SFR, η and Λ, respectively (so that $\dot{M}_{loss} = \eta \times SFR$ and $\dot{M}_{acc} = \Lambda \times SFR$). The outflowing gas in the models has the same metallicity as the remaining gas reservoir, and we always consider pristine (metal-free) gas accretion.

We adopt the general solution for these simple models derived by Kudritzki et al. (2015) (hereafter K15) and relating the oxygen mass fraction O_m (defined as the mass fraction of oxygen in the ISM: $O_m = M_O/M_{gas}$) and the gas fraction f_{gas}:

$$O_m(t) = \frac{y_O}{\Lambda}\left(1 - \left[\frac{(1+\alpha)}{f_{gas}} - \alpha\right]^\omega\right) \tag{12}$$

where: $\omega = \Lambda/((1 - R)(1 + \alpha))$, α is defined as $\alpha = (\eta - \Lambda)/(1 - R)$, t is the time, and R is the fraction of stellar mass returned to the ISM through stellar winds, which is assumed here to have a constant value $R = 0.18$ (Ascasibar et al. 2015; Sánchez Almeida et al. 2015). The factor y_O is the oxygen yield, that is, the mass of oxygen ejected by a generation of stars divided by the mass of the same generation that remains in stellar remnants and long-lived stars.

Closed-box models correspond to $\Lambda = 0$ and $\eta = 0$. In this case, the equation relating O_m and f_{gas} is simpler (K15):

$$O_m(t) = \frac{y_O}{(1 - R)}\ln\left(\frac{1}{f_{gas}}\right). \tag{13}$$
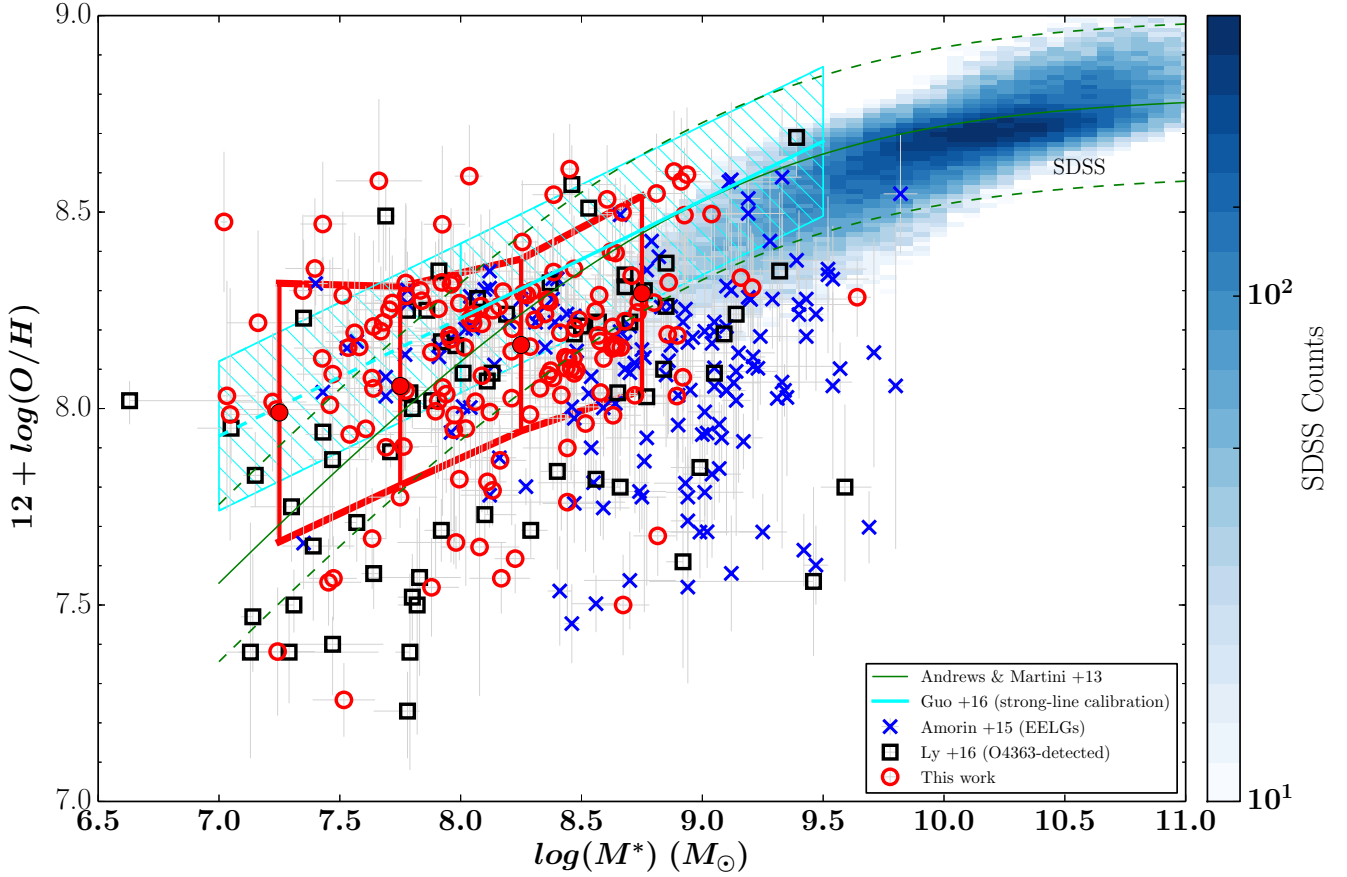
Fig. 20. Comparison between the MZR derived for VUDS SFDGs (red circles) with the mass-metallicity diagram for the galaxy samples compiled by Ly et al. (2016b) (black squares) and Amorín et al. (2015) (blue crosses). We show the best-fit MZR with 1σ uncertainties (cyan continuous lines) of Guo et al. (2016a), plotted for stellar masses $<10^{9.5}$ $M_\odot$ and extrapolated down to 10^7 $M_\odot$ (dashed line). The MZR by Andrews & Martini (2013) with $\pm1\sigma$ uncertainty are shown with green lines and the SDSS galaxies are presented in a 2D histogram with a number density color-bar.

In open box models where only outflows of gas are allowed, $\Lambda = 0$ and $\eta \neq 0$ and Eq. (12) is not defined, so we apply the following expression (K15):

$$O_m(t) = \frac{y_O}{(1-R)}\left(\frac{1}{1+\eta/(1-R)}\ln\left[\frac{1}{f_{\text{gas}}}\left(1+\frac{\eta}{1-R}\right)-\frac{\eta}{1-R}\right]\right).$$

(14)

In order to obtain equations that are consistent with the metallicity used in this paper (i.e., the oxygen abundance defined in terms of number densities, $12 + \log(N(O)/N(H))$, we use $N(O)/N(H) = O_m \times M_{\text{gas}}/(16 M_H)$ (from K15), assuming that $M_{\text{gas}} \sim 1.35 \times M_H$, which takes into account the contribution of helium (Ascasibar et al. 2015).

In Fig. 21, we show three different regions representing a closed-box model with typical oxygen yields for SF galaxies ranging $0.006 < y_O < 0.010$ (Zahid et al. 2012a) (red area), and a model considering outflows only, with varying y_O and for different outflow rates in the range $2 < \eta < 4$ (Wuyts et al. 2012; Sánchez Almeida et al. 2015). In the last case, we also include inflows of pristine gas, choosing a fixed inflow rate of $\Lambda = \eta + 0.95$ (Wuyts et al. 2012) and changing y_O in the same intervals of other models. At high f_{gas}, the different regions overlap and all three models are equally possible, while at lower f_{gas} they separate, allowing us to discriminate between the three regimes.

The distribution of our galaxies shows that they populate a large region in the $12+\log(O/H)$-f_{gas} plane, both at high and low gas fractions. As we mention above, SFDGs at higher f_{gas} can be
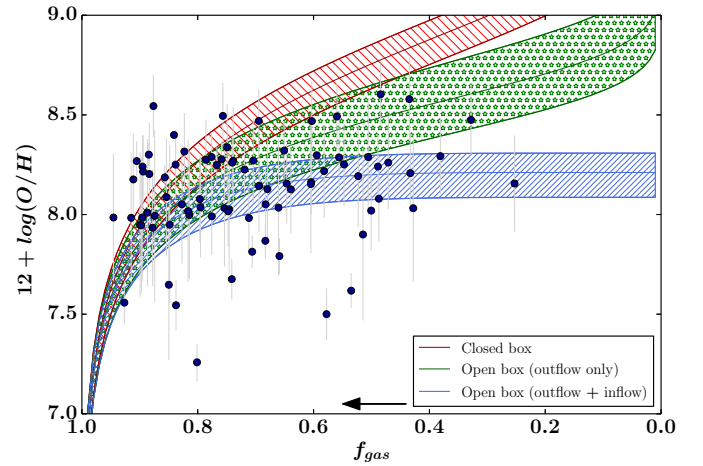
Fig. 21. Diagram relating the metallicity $12 + \log(O/H)$ and the gas fraction f_{gas} for our subsample of SFDGs. The curves represent: (red) closed-box model with oxygen yield $y_O = 0.008$ (0.006–0.010); (green) open box model with outflows for $y_O = 0.008$ (0.006–0.010) and outflow rate $\eta = 3.2$ (Sánchez Almeida et al. 2015) ($2 < \eta < 4$); (blue) open box model with outflows and inflows, choosing $y_O = 0.008$ (0.006–0.010), $\eta = 3.2$ and inflow rate $\Lambda = \eta + 0.95$. As discussed in the text, we acknowledge an average error for f_{gas} of ~0.2 dex.

reproduced equally well by any of the three models. They may still be in an early stage of their evolution where few amounts of

gas have been converted into stars, or simply the star formation proceeds slowly in these systems consuming the gas reservoir over long timescales. On the opposite side, at low f_{gas} ($\lesssim 0.8$), our galaxies show metallicities that are too low to be reproduced by a wide range of closed-box models with physically motivated oxygen yields taken from the literature. All galaxies at lower f_{gas} are consistent with open box models allowing the galaxies to exchange gas with their environment, with a slight preference for "outflow+inflow" models. Unless we choose very high outflow rates η, which are allowed, in principle, according to recent models ($2 < \eta < 100$ is reported in Ascasibar et al. 2015), or we appreciably decrease the value of the oxygen yield y_O; the SFDGs with the lowest metallicity can be explained only by assuming the presence of nearly-pristine inflows of gas occurring at a constant rate.

We also notice that some galaxies lie on the left of the closed-box model, in a phase-space that is not allowed in principle, because interactions with the environment through metal-rich outflows or metal-poor inflows always decrease the metallicity of the ISM compared to an isolated galaxy (which gives the highest possible value). The latter result was also found by other similar works on $z \sim 1$ and $M_* \sim 10^9 M_\odot$ SF galaxies (e.g., Wuyts et al. 2012) and, assuming that the metallicity is correct within the uncertainties, it could be due, in our case, to the large errors on the gas fractions. Considering a typical uncertainty of ~0.2 dex or even higher (difficult to quantify and resulting from a combination of the assumptions made in Eq. (5), the KS law and the measurement of r_e), the points may shift to higher f_{gas} and so they become compatible with the models. On the other hand, some SFDGs show lower abundances at fixed f_{gas} compared to the bulk of our SFDGs. We checked that those galaxies below the "outflow+inflow" model with $12 + \log(O/H) < 7.9$ are all EELGs.

Because of the crucial role of the gas fraction, direct measurements of the gas mass M_{gas} for our galaxies (as already discussed in Sect. 4.4.1) are certainly needed to improve the constraint of analytical models from the observations, and, in general, to reduce the uncertainty on both the slope and the normalization on the KS law for SFDGs below $z \sim 1$. We also remind the reader that we are considering simple scenarios of chemical evolution and more sophisticated models, e.g., considering the additional effect of metal-enriched gas inflows (e.g., Spitoni et al. 2010) or relaxing the instantaneous mixing and recycling approximation, will certainly help to understand the role of our SFDGs in cosmic evolution.

This analysis suggests that open-box models are in stronger agreement with our observations compared to closed-box models. However, we remark the large uncertainties of f_{gas} and the need for direct measurements of HI content for VUDS SFDGs.

6.2. Implications for reionization studies

Large efforts are currently being invested to identify the first luminous sources which reionized the neutral intergalactic medium at redshifts higher than 6 (e.g., Pentericci et al. 2014; Robertson et al. 2015; Giallongo et al. 2015; Grazian et al. 2016). One of the main contributors to cosmic reionization are faint SFDGs with a significant fraction of escaping Lyman continuum photons (i.e., emission at wavelengths $\lambda < 912$ Å). Although this is still an open question, SFDGs could be the best representatives of the LyC leaking galaxies, since the observed faint-end UV LF appears to be steeper at high-z (e.g., Bouwens et al. 2015), and they can contribute more than 20% of
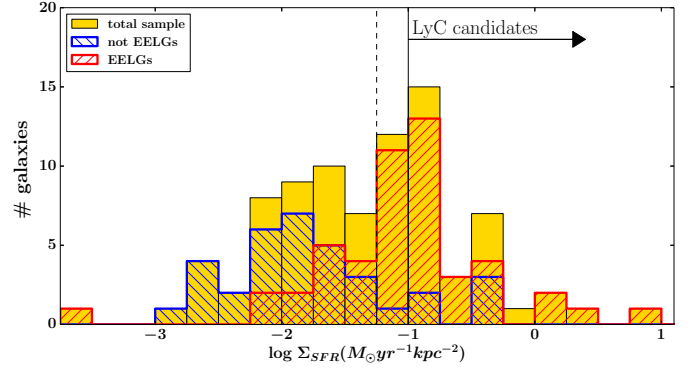
Fig. 22. Histogram of $\log(\Sigma_{SFR})$ for VUDS SFDGs, showing the limit for outflows (Sharma et al. 2017) with a blue dotted vertical line. The majority of the galaxies are included in the range $0.001 < \Sigma_{SFR} < 1$, with a few outliers on both sides. In particular, we find two galaxies with very high Σ_{SFR}, 1.4 and 2.9 $M_\odot$ yr^{-1} kpc^{-2}, respectively.

the total ionizing flux (Dressler et al. 2015; Vanzella et al. 2016). However, direct observations of the LyC photons are extremely challenging and only a few direct detections have been found at low (e.g., Izotov et al. 2016) and intermediate ($z \sim 3$) redshift (de Barros et al. 2016; Vanzella et al. 2016).

In recent years, local candidates for LyC leakers have been selected among EELGs (e.g., Green Peas; Jaskot & Oey 2014), which later turned out to yield successful detections using UV spectroscopy (Izotov et al. 2016). They have similar properties to those expected at very high redshift, namely strong emission lines (with high EW) in the optical spectra, low masses, small sizes, low metallicities and high ionizations, as well as strongly ionized outflows, which appear ubiquitous amongst galaxies with high SFR per unit area ($\Sigma_{SFR} \geq 0.1 M_\odot$ yr^{-1} kpc^{-2}; Heckman et al. 2011; Sharma et al. 2017). Many of these properties have also been found in a fraction of our VUDS SFDGs.

In our sample, 30 SFDGs show Σ_{SFR} (calculated as Eq. (7) and assuming Chabrier 2003, IMF) higher than the lower limit of the range required to produce strong outflows mentioned before, as shown in Fig. 22. The majority (25) of this subset comprises EELGs, which could be the best candidates for LyC leakers in our VUDS sample. Furthermore, 7 EELGs with enhanced Σ_{SFR} also simultaneously present high $EW(H\beta)$ (>100 Å) and high [O III]5007/[O II]3727 ratio (>4), which suggests a very young starburst episode.

Additional constraints on the escape fraction f_{esc} of ionizing radiation can come from the stacking of GALEX data available for all our COSMOS galaxies. A spectroscopic follow-up in the UV rest-frame could also be a good option for future works, focused on the Lyman continuum and Ly-α emission line properties of low-z analogs of those primeval faint SFDGs that are believed to be responsible of reionization during the first Myr after the Big Bang.

7. Summary and conclusions

Our work investigates a sample of star-forming dwarf galaxies (SFDGs) down to $M_* \sim 10^7 M_\odot$ at intermediate redshift, selected from the VUDS spectroscopic survey by the presence of optical emission lines. From their spectra and ancillary photometric data, we have derived important physical properties for this sample (e.g., mass, star-formation rates, metallicity, ionization and sizes), adding new constraints to the low-mass end of the mass-metallicity relation. We have studied simple scenarios

of chemical evolution in a crucial phase of the cosmic stellar mass assembly. Our main findings are summarized as follows:

1. From the three fields of VUDS survey (COSMOS, ECDFS and VVDS-02h), we have selected a sample of 164 star-forming dwarf galaxies at intermediate redshift ($0.13 < z < 0.88$) with detection of the following emission lines: [O III]$\lambda3727$ Å, [O III]$\lambda5007$ Å, Hβ and Hα. We additionally detected the auroral line [O III]$\lambda4363$ Å in 19 galaxies from this sample, and we find that 56% are EELGs, according to the definition $EW($[O III]$\lambda5007 > 100$ Å.

2. Using deep multi-wavelength data available in the three VUDS fields, we have derived stellar masses for the selected galaxies, confirming their low values ranging $10^7 \leq M_*/M_\odot \leq 10^9$. Star-formation rates from Hα luminosity after corrections for dust attenuation and extinction lie in the range $10^{-3} \lesssim SFR \lesssim 10^1$ $M_\odot$/yr (Chabrier IMF). Combining the two measurements, we find that our sample is representative of higher SFRs ($\sim$+0.5 dex), on average, compared to the mean star-forming population (i.e., the SF MS) at similar redshift.

3. We used a novel methodology (HCm), based on the comparison of optical emission line ratios and detailed photoionization models, to derive the metallicity and ionization parameter. Its robustness has been successfully tested against the direct method and other consistent strong-line methods. Applying HCm to our SFDGs, we find that they have low metallicities ranging $7.26 < 12 + \log(O/H) < 8.7$ (0.04–1 $Z_\odot$) and ionization parameters in the range $-3.2 < \log(U) < -1.5$. We find 12 extremely metal-poor ($Z < 0.1\,Z_\odot$) galaxies in our sample.

4. We performed a morphological classification of VUDS SFDGs in COSMOS and ECDFS (101), for which high-resolution ($\sim$0.09″) HST-ACS images are available in these two fields. EELGs have, on average, more disturbed morphologies (cometary, clumpy shapes and interacting-merging systems) compared to the remaining population.

5. Using GALFIT to fit the HST images available for a subset of VUDS SFDGs, we find that they are very compact overall, with a median effective radius $r_e = 1.23$ kpc. They are also gas-rich systems, with a median gas fraction (defined as $f_{gas} = M_{gas}/(M_* + M_{gas})$) of 0.74, derived by inverting an assumedly non-variable Kennicutt-Schmidt law with exponent $n = 1.4$. Despite the large uncertainties of the gas fraction measurements resulting from both the KS law and the size error bars, we highlighted the importance of direct estimations of the HI content in galaxies for more precise estimations of f_{gas}, which may be addressed in our future work.

6. We have added new constraints to the low-mass end ($M_* < 10^9$ $M_\odot$) of the MZR. The MZR of VUDS SFDGs is generally consistent with the local relation of Andrews & Martini (2013), but it shows a flatter slope that is in better agreement with Lee et al. (2006) and Guo et al. (2016a) for local and intermediate redshift SFDGs, respectively. The average dispersion of our sample is $\sim$0.26 dex, and it shows an increasing trend toward lower masses, also found in previous studies at similar redshift (Zahid et al. 2012b; Guo et al. 2016a). We find that below 10^8 $M_\odot$, more metal-poor galaxies show higher sSFRs, while at higher masses, this differentiation vanishes. This dependence at lower masses indicates that sSFR is partly responsible for the moderate slope and for the increasing scatter of our mass-metallicity relation toward $M_* \sim 10^7$ $M_\odot$, in agreement with recent theoretical works (e.g., Lilly et al. 2013).

7. We compared our results with the predictions of simple chemical evolution models. Our data suggest that a closed-box model is not sufficient to reproduce the distribution of our galaxies in the metallicity-f_{gas} plane, while they are more consistent with open-box models (including both outflows and inflows). Quantitative measurements of the total gas content, as well as more sophisticated models, would help to better constrain and fully investigate the chemical evolution of our SFDGs.

8. In our sample, we have found 30 promising candidates to LyC leakers having star-formation surface densities $\Sigma_{SFR} > 0.1$ $M_\odot$ yr^{-1} kpc^{-2}. From these, seven candidates are compact EELGs with $EW($H$\beta) > 100$ Å and $EW($[O III]$5007) > 300$ Å, characterized by high SSFR, low metallicity, and high ionization, as probed by their unusually high (>4) [OIII]5007/[OII]3727 ratios.

References

Abazajian, K. N., Adelman-McCarthy, J. K., Agüeros, M. A., et al. 2009, ApJS, 182, 543
Amorín, R. O., Aguerri, J. A. L., Cairós, L. M., Caon, N., & Muñoz-Tuñón, C. 2007, Galaxy Evolution across the Hubble Time, 235, 300
Amorín, R., Aguerri, J. A. L., Muñoz-Tuñón, C., & Cairós, L. M. 2009, A&A, 501, 75
Amorín, R. O., Pérez-Montero, E., & Vílchez, J. M. 2010, ApJ, 715, L128
Amorín, R., Pérez-Montero, E., Vílchez, J. M., & Papaderos, P. 2012, ApJ, 749, 185
Amorín, R., Sommariva, V., Castellano, M., et al. 2014, A&A, 568, L8
Amorín, R., Pérez-Montero, E., Contini, T., et al. 2015, A&A, 578, A105
Amorín, R., Muñoz-Tuñón, C., Aguerri, J. A. L., & Planesas, P. 2016, A&A, 588, A23
Andrews, B. H., & Martini, P. 2013, ApJ, 765, 140
Ascasibar, Y., Gavilán, M., Pinto, N., et al. 2015, MNRAS, 448, 2126
Asplund, M., Grevesse, N., Sauval, A. J., & Scott, P. 2009, ARA&A, 47, 481
Atek, H., Siana, B., Scarlata, C., et al. 2011, ApJ, 743, 121
Baldwin, J. A., Phillips, M. M., & Terlevich, R. 1981, PASP, 93, 5
Bielby, R., Hudelot, P., McCracken, H. J., et al. 2012, A&A, 545, A23
Bolzonella, M., Kovač, K., Pozzetti, L., et al. 2010, A&A, 524, A76
Bothwell, M. S., Maiolino, R., Kennicutt, R., et al. 2013, MNRAS, 433, 1425
Boulade, O., Charlot, X., Abbon, P., et al. 2003, Proc. SPIE, 4841, 72
Bouwens, R. J., Illingworth, G. D., Oesch, P. A., et al. 2015, ApJ, 811, 140
Brinchmann, J., Charlot, S., White, S. D. M., et al. 2004, MNRAS, 351, 1151
Bruzual, G., & Charlot, S. 2003, MNRAS, 344, 1000
Cairós, L. M., Caon, N., García-Lorenzo, B., et al. 2007, ApJ, 669, 251
Calzetti, D., Armus, L., Bohlin, R. C., et al. 2000, ApJ, 533, 682
Cappelluti, N., Brusa, M., Hasinger, G., et al. 2009, A&A, 497, 635
Cappelluti, N., Comastri, A., Fontana, A., et al. 2016, ApJ, 823, 95
Cardamone, C., Schawinski, K., Sarzi, M., et al. 2009, MNRAS, 399, 1191

Cardamone, C. N., van Dokkum, P. G., Urry, C. M., et al. 2010, ApJS, 189, 270
Cardelli, J. A., Clayton, G. C., & Mathis, J. S. 1989, ApJ, 329, L33
Ceverino, D., Dekel, A., Tweed, D., & Primack, J. 2015, MNRAS, 447, 3291
Chabrier, G. 2003, PASP, 115, 763
Charlot, S., & Longhetti, M. 2001, MNRAS, 323, 887
Chen, T.-W., Smartt, S. J., Bresolin, F., et al. 2013, ApJ, 763, L28
Chiappetti, L., Clerc, N., Pacaud, F., et al. 2013, MNRAS, 429, 1652
Christensen, L., Richard, J., Hjorth, J., et al. 2012, MNRAS, 427, 1953
Civano, F., Elvis, M., Brusa, M., et al. 2012, ApJS, 201, 30
Cuillandre, J.-C. J., Withington, K., Hudelot, P., et al. 2012, Proc. SPIE, 8448, 84480
Cullen, F., Cirasuolo, M., McLure, R. J., Dunlop, J. S., & Bowler, R. A. A. 2014, MNRAS, 440, 2300
Curti, M., Cresci, G., Mannucci, F., et al. 2017, MNRAS, 465, 1384
Daddi, E., Dickinson, M., Morrison, G., et al. 2007, ApJ, 670, 156
Damen, M., Labbé, I., van Dokkum, P. G., et al. 2011, ApJ, 727, 1
Dalcanton, J. J., Yoachim, P., & Bernstein, R. A. 2004, ApJ, 608, 189
Davé, R., Finlator, K., & Oppenheimer, B. D. 2012, MNRAS, 421, 98
de Barros, S., Vanzella, E., Amorín, R., et al. 2016, A&A, 585, A51
Dekel, A., & Woo, J. 2003, MNRAS, 344, 1131
Denicoló, G., Terlevich, R., & Terlevich, E. 2002, MNRAS, 330, 69
Dressler, A., Henry, A., Martin, C. L., et al. 2015, ApJ, 806, 19
Elbaz, D., Daddi, E., Le Borgne, D., et al. 2007, A&A, 468, 33
Ellison, S. L., Patton, D. R., Simard, L., & McConnachie, A. W. 2008, ApJ, 672, L107
Elvis, M., Civano, F., Vignali, C., et al. 2009, ApJS, 184, 158
Erb, D. K., Shapley, A. E., Pettini, M., et al. 2006, ApJ, 644, 813
Ferland, G. J., Porter, R. L., van Hoof, P. A. M., et al. 2013, Rev. Mex. Astron. Astrofís., 49, 137
Filho, M. E., Sánchez Almeida, J., Amorín, R., et al. 2016, ApJ, 820, 109
Finlator, K., & Davé, R. 2008, MNRAS, 385, 2181
Fontana, A., Salimbeni, S., Grazian, A., et al. 2006, A&A, 459, 745
Forbes, J. C., Krumholz, M. R., Burkert, A., & Dekel, A. 2014, MNRAS, 443, 168
Garilli, B., Fumana, M., Franzetti, P., et al. 2010, PASP, 122, 827
Gawiser, E., van Dokkum, P. G., Herrera, D., et al. 2006, ApJS, 162, 1
Giallongo, E., Grazian, A., Fiore, F., et al. 2015, A&A, 578, A83
Gil de Paz, A., & Madore, B. F. 2005, ApJS, 156, 345
Grazian, A., Fontana, A., Santini, P., et al. 2015, A&A, 575, A96
Grazian, A., Giallongo, E., Gerbasi, R., et al. 2016, A&A, 585, A48
Guo, K., Zheng, X. Z., Wang, T., & Fu, H. 2015, ApJ, 808, L49
Guo, Y., Koo, D. C., Lu, Y., et al. 2016a, ApJ, 822, 103
Guo, Y., Rafelski, M., Faber, S. M., et al. 2016b, ApJ, 833, 37
Guzmán, R., Gallego, J., Koo, D. C., et al. 1997, ApJ, 489, 559
Hägele, G. F., Díaz, Á. I., Terlevich, E., et al. 2008, MNRAS, 383, 209
Heckman, T. M., Borthakur, S., Overzier, R., et al. 2011, ApJ, 730, 5
Henry, A., Scarlata, C., Domínguez, A., et al. 2013, ApJ, 776, L27
Hopkins, P. F., Kereš, D., Oñorbe, J., et al. 2014, MNRAS, 445, 581
Hughes, T. M., Cortese, L., Boselli, A., Gavazzi, G., & Davies, J. I. 2013, A&A, 550, A115
Ilbert, O., Tresse, L., Zucca, E., et al. 2005, A&A, 439, 863
Ilbert, O., Arnouts, S., McCracken, H. J., et al. 2006, A&A, 457, 841
Ilbert, O., Capak, P., Salvato, M., et al. 2009, ApJ, 690, 1236
Ilbert, O., McCracken, H. J., Le Fèvre, O., et al. 2013, A&A, 556, A55
Izotov, Y. I., & Thuan, T. X. 1999, ApJ, 511, 639
Izotov, Y. I., Guseva, N. G., Fricke, K. J., & Henkel, C. 2015, MNRAS, 451, 2251
Izotov, Y. I., Schaerer, D., Thuan, T. X., et al. 2016, MNRAS, 461, 3683
Jaskot, A. E., & Oey, M. S. 2013, ApJ, 766, 91
Jaskot, A. E., & Oey, M. S. 2014, in Massive Young Star Clusters Near and Far: From the Milky Way to Reionization, 2013 Guillermo Haro Conf. (INAOE & AMC), 171
Juneau, S., Dickinson, M., Alexander, D. M., & Salim, S. 2011, ApJ, 736, 104
Juneau, S., Bournaud, F., Charlot, S., et al. 2014, ApJ, 788, 88
Kakazu, Y., Cowie, L. L., & Hu, E. M. 2007, ApJ, 668, 853
Karachentsev, I. D., Karachentseva, V. E., Huchtmeier, W. K., & Makarov, D. I. 2004, AJ, 127, 2031
Kauffmann, G., Heckman, T. M., White, S. D. M., et al. 2003, MNRAS, 341, 33
Kennicutt, R. C., & Evans, N. J. 2012, ARA&A, 50, 531
Kennicutt, R. C., Jr. 1998, ARA&A, 36, 189
Kewley, L. J., & Dopita, M. A. 2002, ApJS, 142, 35
Kewley, L. J., & Ellison, S. L. 2008, ApJ, 681, 1183
Kniazev, A. Y., Pustilnik, S. A., Grebel, E. K., Lee, H., & Pramskij, A. G. 2004, ApJS, 153, 429
Kobayashi, C., Springel, V., & White, S. D. M. 2007, MNRAS, 376, 1465
Kobulnicky, H. A., Willmer, C. N. A., Phillips, A. C., et al. 2003, ApJ, 599, 1006
Koekemoer, A. M., Aussel, H., Calzetti, D., et al. 2007, ApJS, 172, 196
Kudritzki, R.-P., Ho, I.-T., Schruba, A., et al. 2015, MNRAS, 450, 342
Kunth, D., & Östlin, G. 2000, A&ARv, 10, 1
Lamareille, F., Mouhcine, M., Contini, T., Lewis, I., & Maddox, S. 2004, MNRAS, 350, 396
Lara-López, M. A., Cepa, J., Bongiovanni, A., et al. 2010, A&A, 521, L53
Lara-López, M. A., Hopkins, A. M., López-Sánchez, A. R., et al. 2013, MNRAS, 433, L35
Le Fevre, O., Vettolani, G., Maccagni, D., et al. 2003, Proc. SPIE, 4834, 173
Le Fèvre, O., Tasca, L. A. M., Cassata, P., et al. 2015, A&A, 576, A79
Lee, H., Skillman, E. D., Cannon, J. M., et al. 2006, ApJ, 647, 970
Lehmer, B. D., Brandt, W. N., Alexander, D. M., et al. 2005, ApJS, 161, 21
Leloudas, G., Schulze, S., Krühler, T., et al. 2015, MNRAS, 449, 917
Lequeux, J., Peimbert, M., Rayo, J. F., Serrano, A., & Torres-Peimbert, S. 1979, A&A, 80, 155
Leroy, A., Bolatto, A. D., Simon, J. D., & Blitz, L. 2005, ApJ, 625, 763
Lilly, S. J., Carollo, C. M., Pipino, A., Renzini, A., & Peng, Y. 2013, ApJ, 772, 119
López-Sánchez, Á. R., Dopita, M. A., Kewley, L. J., et al. 2012, MNRAS, 426, 2630
Lunnan, R., Chornock, R., Berger, E., et al. 2013, ApJ, 771, 97
Luo, B., Bauer, F. E., Brandt, W. N., et al. 2008, ApJS, 179, 19
Ly, C., Malkan, M. A., Nagao, T., et al. 2014, ApJ, 780, 122
Ly, C., Rigby, J. R., Cooper, M., & Yan, R. 2015, ApJ, 805, 45
Ly, C., Malhotra, S., Malkan, M. A., et al. 2016a, ApJS, 226, 5
Ly, C., Malkan, M. A., Rigby, J. R., & Nagao, T. 2016b, ApJ, 828, 67
Madau, P., & Dickinson, M. 2014, ARA&A, 52, 415
Maiolino, R., Nagao, T., Grazian, A., et al. 2008, A&A, 488, 463
Mannucci, F., Cresci, G., Maiolino, R., et al. 2009, MNRAS, 398, 1915
Mannucci, F., Cresci, G., Maiolino, R., Marconi, A., & Gnerucci, A. 2010, MNRAS, 408, 2115
Mannucci, F., Salvaterra, R., & Campisi, M. A. 2011, MNRAS, 414, 1263
Marino, R. A., Rosales-Ortega, F. F., Sánchez, S. F., et al. 2013, A&A, 559, A114
Maseda, M. V., van der Wel, A., Rix, H.-W., et al. 2014, ApJ, 791, 17
Mauduit, J.-C., Lacy, M., Farrah, D., et al. 2012, PASP, 124, 714
McGaugh, S. S. 1991, ApJ, 380, 140
Mollá, M., García-Vargas, M. L., & Bressan, A. 2009, MNRAS, 398, 451
Moustakas, J., Kennicutt, R. C., Jr., Tremonti, C. A., et al. 2010, ApJS, 190, 233
Nagao, T., Maiolino, R., & Marconi, A. 2006, A&A, 459, 85
Nakajima, K., & Ouchi, M. 2014, MNRAS, 442, 900
Noeske, K. G., Weiner, B. J., Faber, S. M., et al. 2007, ApJ, 660, L43
Olmo-Garcia, A., Sanchez Almeida, J., Munoz-Tunon, C., et al. 2017, ApJ, 834, 181
Onodera, M., Carollo, C. M., Lilly, S., et al. 2016, ApJ, 822, 42
Osterbrock, D. E. 1989, Astrophysics of Gaseous Nebulae and Active Galactic Nuclei. University of Minnesota (Mill Valley, CA: University Science Books)
Papaderos, P., & Östlin, G. 2012, A&A, 537, A126
Papaderos, P., Loose, H.-H., Thuan, T. X., & Fricke, K. J. 1996, A&AS, 120, 207
Peeples, M. S., Pogge, R. W., & Stanek, K. Z. 2008, ApJ, 685, 904
Pelupessy, F. I., van der Werf, P. P., & Icke, V. 2004, A&A, 422, 55
Peng, C. Y., Ho, L. C., Impey, C. D., & Rix, H.-W. 2002, AJ, 124, 266
Peng, C. Y., Ho, L. C., Impey, C. D., & Rix, H.-W. 2010, AJ, 139, 2097
Pentericci, L., Vanzella, E., Fontana, A., et al. 2014, ApJ, 793, 113
Pérez-Montero, E. 2014, MNRAS, 441, 2663
Pérez-Montero, E., & Contini, T. 2009, MNRAS, 398, 949
Pérez-Montero, E., & Díaz, A. I. 2005, MNRAS, 361, 1063
Pérez-Montero, E., Contini, T., Lamareille, F., et al. 2013, A&A, 549, A25
Pettini, M., & Pagel, B. E. J. 2004, MNRAS, 348, L59
Pierre, M., Valtchanov, I., Altieri, B., et al. 2004, J. Cosmology Astropart. Phys., 9, 011
Pilyugin, L. S., Vílchez, J. M., Cedrés, B., & Thuan, T. X. 2010, MNRAS, 403, 896
Press, W. H., & Schechter, P. 1974, ApJ, 187, 425
Reddy, N. A., Erb, D. K., Pettini, M., Steidel, C. C., & Shapley, A. E. 2010, ApJ, 712, 1070
Ribeiro, B., Le Fèvre, O., Tasca, L. A. M., et al. 2016, A&A, 593, A22
Robertson, B. E., Ellis, R. S., Furlanetto, S. R., & Dunlop, J. S. 2015, ApJ, 802, L19
Rola, C. S., Terlevich, E., & Terlevich, R. J. 1997, MNRAS, 289, 419
Salim, S., Lee, J. C., Ly, C., et al. 2014, ApJ, 797, 126
Sánchez Almeida, J., Elmegreen, B. G., Muñoz-Tuñón, C., & Elmegreen, D. M. 2014a, A&ARv, 22, 71
Sánchez Almeida, J., Morales-Luis, A. B., Muñoz-Tuñón, C., et al. 2014b, ApJ, 783, 45
Sánchez Almeida, J., Elmegreen, B. G., Muñoz-Tuñón, C., et al. 2015, ApJ, 810, L15
Sánchez, S. F., Kennicutt, R. C., Gil de Paz, A., et al. 2012, A&A, 538, A8
Sánchez, S. F., Rosales-Ortega, F. F., Jungwiert, B., et al. 2013, A&A, 554, A58

Sánchez-Janssen, R., Amorín, R., García-Vargas, M., et al. 2013, A&A, 554, A20

Santini, P., Fontana, A., Grazian, A., et al. 2009, A&A, 504, 751

Santini, P., Fontana, A., Grazian, A., et al. 2012, A&A, 538, A33

Savaglio, S. 2010, Progenitors and Environments of Stellar Explosions, 26th IAP Colloq., 39

Schreiber, C., Pannella, M., Elbaz, D., et al. 2015, A&A, 575, A74

Scoville, N., Aussel, H., Brusa, M., et al. 2007, ApJS, 172, 1

Sérsic, J. L. 1968, Boletin de la Asociacion Argentina de Astronomia La Plata Argentina, 13, 20

Shapley, A. E., Coil, A. L., Ma, C.-P., & Bundy, K. 2005, ApJ, 635, 1006

Sharma, M., Theuns, T., Frenk, C., et al. 2017, MNRAS, 468, 2176

Smit, R., Bouwens, R. J., Labbé, I., et al. 2014, ApJ, 784, 58

Sparre, M., Hayward, C. C., Feldmann, R., et al. 2017, MNRAS, 466, 88

Spitoni, E., Calura, F., Matteucci, F., & Recchi, S. 2010, A&A, 514, A73

Stark, D. P., Ellis, R. S., Charlot, S., et al. 2017, MNRAS, 464, 469

Stasińska, G. 2010, Stellar Populations, Planning for the Next Decade, IAU Symp., 262, 93

Stasińska, G., Izotov, Y., Morisset, C., & Guseva, N. 2015, A&A, 576, A83

Stoughton, C., Lupton, R. H., Bernardi, M., et al. 2002, AJ, 123, 485

Taniguchi, Y., Scoville, N., Murayama, T., et al. 2007, ApJS, 172, 9

Tasca, L. A. M., Le Fèvre, O., Hathi, N. P., et al. 2015, A&A, 581, A54

Tasca, L. A. M., Le Fevre, O., Ribeiro, B., et al. 2017, A&A, 600, A110

Tassis, K., Kravtsov, A. V., & Gnedin, N. Y. 2008, Dark Galaxies and Lost Baryons, IAU Sump., 244, 256

Taylor, E. N., Franx, M., van Dokkum, P. G., et al. 2009, ApJS, 183, 295

Telford, O. G., Dalcanton, J. J., Skillman, E. D., & Conroy, C. 2016, ApJ, 827, 35

Terlevich, R., Melnick, J., Masegosa, J., Moles, M., & Copetti, M. V. F. 1991, A&AS, 91, 285

Thöne, C. C., de Ugarte Postigo, A., García-Benito, R., et al. 2015, MNRAS, 451, L65

Tremonti, C. A., Heckman, T. M., Kauffmann, G., et al. 2004, ApJ, 613, 898

Troncoso, P., Maiolino, R., Sommariva, V., et al. 2014, A&A, 563, A58

van der Wel, A., Straughn, A. N., Rix, H.-W., et al. 2011, ApJ, 742, 111

Vanzella, E., de Barros, S., Vasei, K., et al. 2016, ApJ, 825, 41

Whitaker, K. E., Franx, M., Leja, J., et al. 2014, ApJ, 795, 104

Wuyts, E., Rigby, J. R., Sharon, K., & Gladders, M. D. 2012, ApJ, 755, 73

Wuyts, S., Förster Schreiber, N. M., Nelson, E. J., et al. 2013, ApJ, 779, 135

Xue, Y. Q., Wang, S. X., Brandt, W. N., et al. 2012, ApJ, 758, 129

Zahid, H. J., Dima, G. I., Kewley, L. J., Erb, D. K., & Davé, R. 2012a, ApJ, 757, 54

Zahid, H. J., Bresolin, F., Kewley, L. J., Coil, A. L., & Davé, R. 2012b, ApJ, 750, 120

Zamojski, M. A., Schiminovich, D., Rich, R. M., et al. 2007, ApJS, 172, 468

Zhao, Y., Gao, Y., & Gu, Q. 2010, ApJ, 710, 663

Appendix A: Derivation of metallicity with other methods

In this section, we explore the main differences and similarities between the metallicities based on the code HCm and those derived with the widely-used strong-line methods. Strong-line methods are based on the physical properties of HII regions, in which a relation has been found between emission-line intensities and oxygen abundances (see Pérez-Montero & Díaz 2005). The calibrations can be derived empirically or through photoionization models. Empirical calibrations are provided by many authors, e.g., Pettini & Pagel (2004), Marino et al. (2013), Maiolino et al. (2008), Pérez-Montero & Contini (2009). These methods are generally consistent with direct observations but, on the contrary, can be systematically different when good measurements of the O4363 line are available (Stasińska 2010). On the other hand, photoionization models typically require numerous constraints, for example not only the emission line ratios, but also the stellar content and the nebular gas distribution. One important problem is that many of the most widely used calibrations based on photoionization models (e.g., McGaugh 1991; Kewley & Dopita 2002) also give systematic overabundances with respect to the direct method. These differences can be up to 0.7 dex depending on the models and the Z range (Kewley & Ellison 2008; Moustakas et al. 2010; Stasińska 2010; López-Sánchez et al. 2012).

In this work, we compare our results with the calibrations of Maiolino et al. (2008), McGaugh (1991), Pettini & Pagel (2004), and Marino et al. (2013). After providing a brief description of each method and showing the results, we also provide polynomial fittings, which can be used for conversion between those calibrations and HCm-consistent metallicities. In the following, we check the consistency of the MZR derived in Sect. 5.3 used in various methods for deriving the oxygen abundance.

A.1. Comparison with strong-line calibrations

The method of Maiolino et al. (2008) (M08) is based on two different calibrations for the lower and higher metallicity branches; at high metallicity, $\Delta(12 + \log(O/H)) > 8.35$, it is based on photoionization models from Kewley & Dopita (2002), while at lower metallicity it adopts an empirical calibration derived from a sample of metal-poor galaxies from Nagao et al. (2006) with auroral line detection and T_e-based metallicities. The comparison in Fig. A.1 between M08 metallicities and our values shows some systematic error around $12 + \log(O/H) \simeq 8$, likely due to the R_{23} degeneracy: at metallicities $12 + \log(O/H) \leq 8$, M08 calibrations tend to give lower values ($\sim 0.3-0.4$ dex, with peaks of -0.6 dex) than ours, while at higher metallicities ($8 \leq 12 + \log(O/H) \leq 8.4$), calibrations produce higher values by the same amount. These different trends disappear when we consider the whole metallicity range, and the two medians are very close ($\Delta(12 + \log(O/H)) = 0.05$). The overall dispersion is approximately ~ 0.3 dex in the full range of Z.

The McGaugh (1991) calibration (M91) is based on detailed HII region models. We use the analytic expressions proposed by Kobulnicky et al. (2003), which take into account the dependence of R_{23} on the ionization parameter, and adopts the [N II]/[O II] line ratio to break the R_{23} degeneracy. Then, following Pérez-Montero et al. (2013), we apply a correction to make these R23 metallicities consistent with those calculated through the direct method. In the upper-right part of Fig. A.1, we show the comparison between the results obtained with HCm and the corrected version of M91 calibration (hereafter M91$_{corr}$). Even though both methods are based on similar photoionization models, the dispersion of the points around the 1:1 relation is still significant (~ 0.25 dex). We can find galaxies with $12+\log(O/H)_{HCm}$ around 8 (where R_{23} peaks) having discrepancies with respect to M91$_{corr}$ up to $0.6-0.7$ dex. These discrepancies can be justified both with the way the ionization parameter enters the model estimation and with modifications in the theoretical modeling of stellar atmospheres at higher redshifts, where we find typically more massive and more metal-poor ionizing stars compared to the local Universe.

Finally, PP04 and M13 O3N2 methods were derived independently by Pettini & Pagel (2004) and Marino et al. (2013) to fit the observed relationships between O3N2 parameters, defined as O3N2 = [O III]/Hβ]/([N II]/Hα), and the T_e-based metallicities for samples of extragalactic HII regions. The first adopts the catalog of 137 objects compiled by Denicoló et al. (2002), while M13 include 603 HII regions extracted from the literature (e.g., Pilyugin et al. 2010) and from the CALIFA survey (see Sánchez et al. 2012). Therefore, we can refer to the PP04 and M13 methods as empirical T_e-based calibrations. The comparison of Fig. A.1 (bottom) shows that metallicities derived using PP04 and M13 calibrations span a narrow range: $8.0 \leq (12 + \log(O/H) \leq 8.4$. Even though the dispersion is similar to previous calibrations ($\simeq 0.24$ dex and $\simeq 0.15$), we see that they give systematic overabundances in the low-metallicity range, with differences as high as $\simeq +0.7$ dex at $12 + \log(O/H) < 7.6$.
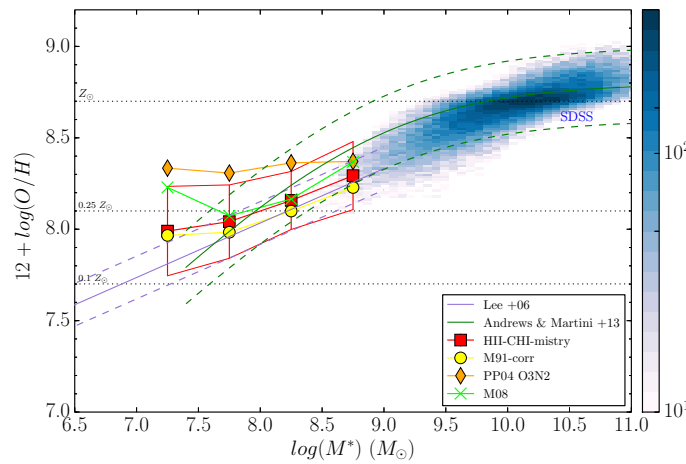
A.2. MZR derived with strong-line methods

We study the effects of using different metallicity calibrations on the mass-metallicity relation. We consider the strong-line methods presented in the previous section (M08, M91, PP04 and M13) and plot the stellar mass versus the new oxygen abundances for each galaxy (see Fig. A.2. As we have seen before, PP04 and M13 give systematic overabundances at lower masses when compared to HCm, therefore their medians are above our 1σ limits. The M08 calibration is mainly consistent with our results, but gives higher abundances (~ 0.25 dex) in the lowest and highest mass bins. Finally, the MZR$_{M91-corr}$ shows a very similar trend to our MZR. Overall, Fig. A.2 shows that choosing a different metallicity calibration affects both the slope and the normalization of the mass-metallicity relation. Even though our MZR greatly overlaps the MZR of AM13 (showing consistent metallicity ranges within the errors at fixed stellar mass), we cannot recover its slope using any of the three other metallicity calibrators. In particular, PP04 and M08 have the opposite effect, with higher abundances toward lower masses.
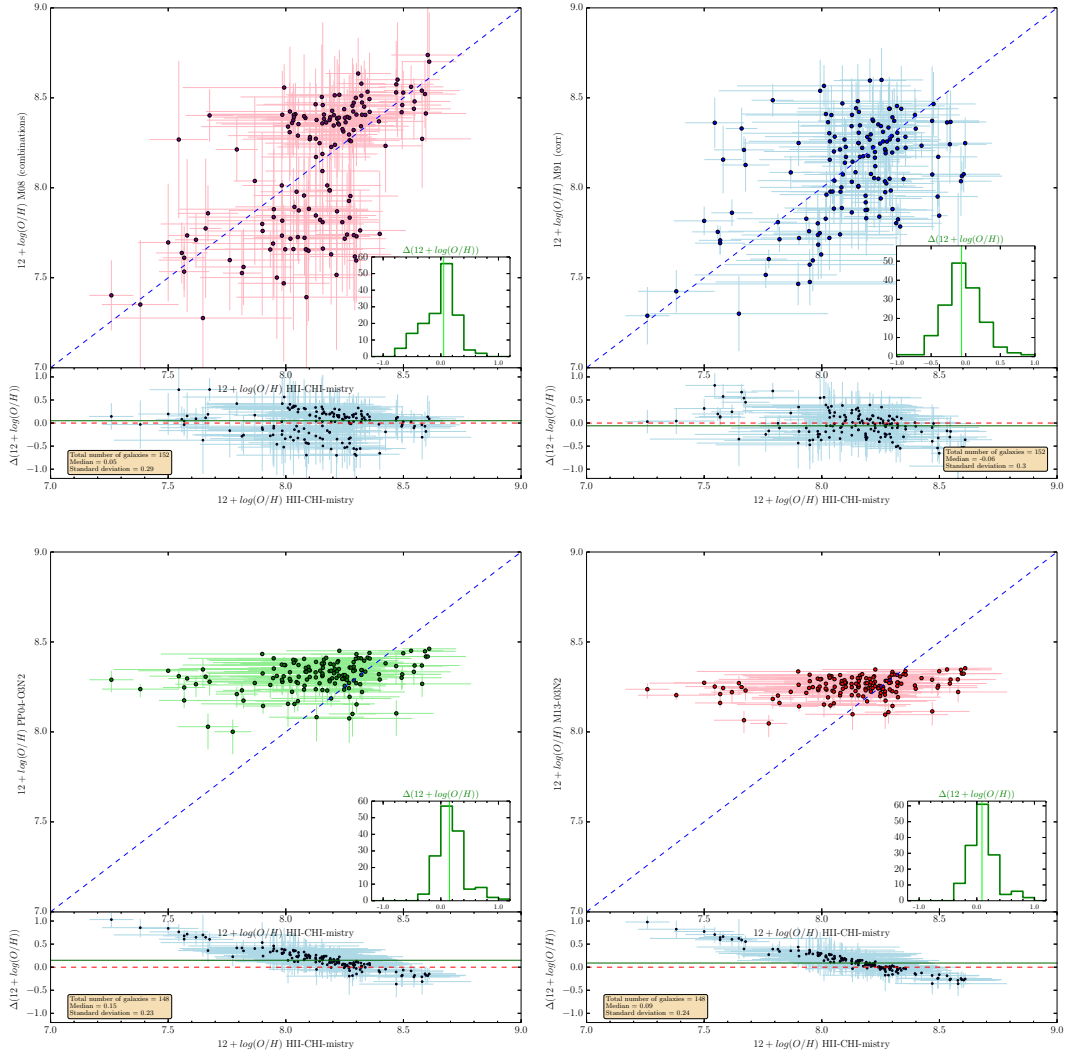
Fig. A.1. Comparison between the metallicity derived with the code HCm and different strong-line calibrations. *Top*: a combination of calibrations by Maiolino et al. (2008) and corrected McGaugh (1991) calibration. *Bottom*: calibrations by Pettini & Pagel (2004) and Marino et al. (2013). A histogram is shown in each panel displaying the difference between the metallicities estimated with each of the four strong-line methods and HCm. In the *bottom part*, the difference is plotted as a function of HCm values.

Fig. A.2. Comparison between the MZR derived with different strong line calibrations: PP04 O3N2 and M13 (orange diamonds), M08 (green crosses) and M91$_{corr}$ (yellow circles). We use the formulation of the M91 calibration given by Kobulnicky et al. (2003), which takes into account the dependence of R_{23} on the ionization parameter. In addition, we correct these metallicities following Pérez-Montero et al. (2013) to make them consistent with those derived using the direct method. We see that HCm and M91 relations show a similar trend in the whole metallicity range. Green lines are the Andrews & Martini (2013) MZR and $\pm 1\sigma$ uncertainties.

Appendix B: Tables

Table B.1. Basic information about VUDS selected galaxies.

VUDS ID (1)	α(J2000) (2)	δ(J2000) (3)	z (4)	i_{AB} (5)	$I_{AB,0}$ (6)	Field (7)
510086862	149.661556	1.872843	0.1268	24.801	−13.522	0
510146174	149.790243	1.988252	0.4781	24.995	−16.689	0
510165275	150.125865	2.0236	0.4787	24.368	−17.282	0
510175664	150.113065	2.042952	0.5018	24.976	−17.181	0
510229076	150.049327	2.137676	0.2197	24.867	−14.698	0
510329403	150.13033	1.772111	0.1845	24.639	−15.012	0
510330378	150.08737	1.763878	0.3374	24.374	−16.478	0
510352169	149.99831	1.786842	0.6282	23.792	−17.877	0
510353245	149.98308	1.782065	0.257	24.527	−15.539	0
510376669	149.877590	1.786568	0.5310	24.573	−16.459	0

Notes. Columns: (1) VUDS identification number; (2) and (3) equatorial coordinates (J2000), right ascension and declination, respectively; (4) VUDS spectroscopic redshift; (5) i-band magnitude, used for the selection of galaxies in VUDS; (6) rest-frame absolute magnitude in the i band coming from SED fitting, as described in Sect. 4.1; (7) VUDS field: 0 = COSMOS, 1 = ECDFS, 2 = VVDS-02h. The entire version of this table for the full sample of SFDGs is available at the CDS.

Table B.2. Emission line fluxes and EWs of selected galaxies in VUDS.

VUDS ID	[O II] λ3727	W([O II])	[Ne III] λ3868	Hγ	[O III] λ4363	Hβ	W([Hβ])	[O III] λ4959	[O III] λ5007	W([O III])	Hα	W(Hα)	[N II] λ6583	[S II] λ6716	[S II] λ6731	c(Hβ)
(1)	(2)	(3)	(4)	(5)	(6)	(7)	(8)	(9)	(10)	(11)	(12)	(13)	(14)	(15)	(16)	(17)
510086862	13.7 ± 1.5	80.3 ± 4	3.4 ± 0.9	–	–	5.5 ± 0.8	31.5 ± 3	3.3 ± 1.0	10.1 ± 1.0	52.0 ± 7.0	12.5 ± 2	80 ± 15	1.5 ± 0.4	–	–	0.078[c]
510146174	9.8 ± 1	158 ± 60	2.1 ± 0.4	3 ± 0.5	–	7.4 ± 1.5	106 ± 37	11.9 ± 1.6	39.6 ± 0.8	560.0 ± 150.0	–	–	–	–	–	0.627[c]
510165275	20.8 ± 1.5	75 ± 13	9.4 ± 0.6	12 ± 1.5	3.2 ± 0.5	23.5 ± 0.7	150 ± 15	35.5 ± 1.5	102.4 ± 1.3	661.0 ± 170.0	–	–	–	–	–	0.229[b]
510175664	12.1 ± 1.4	92 ± 30	4.7 ± 1	–	–	14.7 ± 1.2	135 ± 70	17.1 ± 0.9	48.9 ± 1.2	648.0 ± 250.0	–	–	–	–	–	0.157[c]
510229076	6.4 ± 0.8	49 ± 17	2 ± 0.2	3.3 ± 0.6	–	5.8 ± 1.6	44.5 ± 15	5.4 ± 0.5	17.4 ± 1.4	109.0 ± 36.0	25.1 ± 1.6	116 ± 36	–	4.9 ± 1	0.6 ± 0.4	0.594[a]
510329403	6.8 ± 1.3	59 ± 12	2.5 ± 0.9	–	–	3.6 ± 0.8	12.7 ± 2.7	4.1 ± 0.9	11.4 ± 1.0	37.0 ± 7.0	12 ± 1.5	50 ± 11	–	–	–	0.232[a]
510330378	15 ± 2	130 ± 60	–	3 ± 0.6	–	13.5 ± 1.1	66 ± 13	23.3 ± 1.5	67.5 ± 1.5	274.0 ± 44.0	42 ± 4	260 ± 120	3.7 ± 1.1	–	–	0.136[a]
510352169	26.4 ± 2.6	50 ± 11	29.7 ± 3.4	–	–	50.8 ± 4.0	195 ± 34	94.2 ± 5.0	247.0 ± 3.0	670.0 ± 190.0	–	–	–	–	–	0.47[c]
510353245	12 ± 2	24.3 ± 5	–	–	–	9.0 ± 1.6	25 ± 6	13.0 ± 2.5	39.5 ± 2.5	122.0 ± 24.0	17.1 ± 2	116 ± 46	–	–	–	0.392[c]
510376669	9.9 ± 0.7	44 ± 11	6.6 ± 0.7	7.2 ± 1	3.1 ± 0.4	24.0 ± 1.6	184 ± 60	55.6 ± 1.5	116.0 ± 2.0	950.0 ± 300.0	–	–	–	–	–	0.235[c]

Notes. Columns: (1) VUDS identification number; (2) to (16) Fluxes and EWs of the emission lines measured with the task *splot* of IRAF. The fluxes are given in 10^{-18} erg cm^{-2} s^{-1}, while the equivalent widths (W) are in Å. No extinction correction has been applied to these fluxes. (17) Reddening constant derived from (a) Hα/Hβ or (b) Hγ/Hβ ratios, whenever possible, or (c) the SED best-fitting for those galaxies where (a) and (b) cannot be measured or where they produce a negative extinction (i.e., Hα/Hβ < 2.82 or Hγ/Hβ < 0.47, assuming Case B recombination with $T_e = 2 \times 10^4$ K, $n_e = 100$ cm^{-3}). The entire version of this table for the full sample of ELGs is available at the CDS.

Table B.3. Derived physical properties of intermediate-redshift ELGs in VUDS.

VUDS ID (1)	M_* (2)	SFR (3)	r_e (4)	q (5)	μ_{gas} (6)	f_{gas} (7)	$12 + \log(O/H)$ (8)	$\log(U)$ (9)	MT (10)
510086862	7.02 ± 0.01	−2.459 ± 0.064	0.339 ± 0.016	0.445 ± 0.028	12.06	0.33	8.47 ± 0.18	−3.00 ± 0.08	1
510146174	7.84 ± 0.20	−0.220 ± 0.080	0.498 ± 0.034	0.686 ± 0.054	276.24	0.79	8.27 ± 0.20	−2.49 ± 0.14	0
510165275	7.45 ± 0.14	−0.114 ± 0.013	0.676 ± 0.013	0.268 ± 0.018	212.59	0.93	7.56 ± 0.11	−1.83 ± 0.23	2
510175664	8.44 ± 0.35	−0.337 ± 0.034	−9.9	−9.9	−9.9	−9.9	7.76 ± 0.30	−2.41 ± 0.21	0
510229076	7.03 ± 0.12	−1.206 ± 0.027	0.240 ± 0.013	0.680 ± 0.049	155.08	0.75	8.03 ± 0.29	−2.64 ± 0.19	0
510329403	7.16 ± 0.17	−1.966 ± 0.051	0.902 ± 0.061	0.529 ± 0.028	6.71	0.58	8.22 ± 0.23	−2.68 ± 0.15	4
510330378	7.64 ± 0.21	−0.841 ± 0.040	0.521 ± 0.068	0.692 ± 0.046	93.44	0.68	8.05 ± 0.18	−2.44 ± 0.17	0
510352169	7.99 ± 0.09	0.774 ± 0.033	−9.9	−9.9	−9.9	−9.9	7.82 ± 0.21	−2.20 ± 0.18	1
510353245	7.56 ± 0.13	−1.346 ± 0.048	0.501 ± 0.024	0.649 ± 0.037	43.02	0.52	8.19 ± 0.25	−2.48 ± 0.20	1
510376669	7.47 ± 0.10	0.018 ± 0.028	−9.9	−9.9	−9.9	−9.9	7.57 ± 0.11	−1.69 ± 0.20	0

Notes. (1) VUDS ID; (2) stellar masses (in $\log M_\odot$) and 1σ uncertainties from SED fitting, as described in Sect. 4.1; (3) star formation rates (in $\log(M_\odot$/yr) from Hα or Hβ luminosity assuming Chabrier (2003) IMF and a theoretical ratio Hα/Hβ = 2.82; uncertainties in SFR account for the propagation of errors in line fluxes and reddening; (4) effective radius (in kpc), derived applying GALFIT to $F814W$-band ACS-HST images as described in Sect. 4.4. A value of −9.9 is assigned for those cases in which: (a) GALFIT is not applied (VVDS-02h field) or (b) GALFIT returns an error at the end of the fitting procedure. (5) Ratio between the minor and major axis of the ellipse enclosing half of the total luminosity of the galaxy in the $F814W$ filter; (6) and (7) gas surface density (μ_{gas}, in $M_\odot$ pc^{-2}) and gas fraction f_{gas}, respectively, which were derived from the SFR surface densities assuming a Kennicutt-Schmidt law with exponent 1.4, as described in Sect. 4.4. For μ_{gas} and f_{gas}, we should consider an uncertainty of at least 0.2−0.3 dex (~a factor of two), which comes both from the uncertainties of the size and also from the KS law (which has an average dispersion over different types of galaxies of ~0.2 dex). (8) Gas-phase metallicity derived from the code HII-CHI-mistry. The code also returns an error for the estimation; (9) ionization parameter and its uncertainty derived from HII-CHI-mistry; (10) morphological type as follows: 0 = round/nucleated, 1 = tadpole/cometary, 2 = clumpy/Chain, 3 = merger/interacting, 4 = low surface brightness, 5 = unresolved, 6 = not available (see Sect. 4.4 for more details). The entire version of this table for the whole sample is available at the CDS.